

The Type Ia supernovae rate with Subaru/XMM-Newton Deep Survey

Jun E. Okumura^{1,3}, Yutaka Ihara^{2,3}, Mamoru Doi^{2,4}, Tomoki Morokuma², Reynald Pain⁵, Tomonori Totani^{3,4,1}, Kyle Barbary^{6,7}, Naohiro Takanashi⁸, Naoki Yasuda⁹, Greg Aldering⁷, Kyle Dawson^{7,10}, Gerson Goldhaber^{7,†}, Isobel Hook^{11,12}, Chris Lidman¹³, Saul Perlmutter^{6,7}, Anthony Spadafora⁷, Nao Suzuki^{7,9}, and Lifan Wang¹⁴

¹Department of Astronomy, School of Science, Kyoto University, Sakyo-ku, Kyoto 606-8502

²Institute of Astronomy, University of Tokyo, 2-21-1 Osawa, Mitaka-shi, Tokyo 181-0015

³Department of Astronomy, Graduate School of Science, University of Tokyo, 7-3-1 Hongo, Bunkyo-ku, Tokyo 113-0033

⁴Research Center for the Early Universe, Graduate School of Science, University of Tokyo, 7-3-1 Hongo, Bunkyo-ku, Tokyo 113-0033

⁵LPNHE, CNRS/IN2P3, Université Pierre et Marie Curie, Université Denis Diderot, 4 place Jussieu, 75252 Paris Cedex 05, France

⁶Department of Physics, University of California Berkeley, Berkeley, CA 94720, USA

⁷Lawrence Berkeley National Laboratory, 1 Cyclotron Road, Berkeley, CA 94720, USA

⁸The University of Tokyo Executive Management Program, Ito International Research Center 2nd floor, 7-3-1 Hongo, Bunkyo-ku, Tokyo 113-0033

⁹Kavli Institute for the Physics and Mathematics of the Universe (IPMU), The University of Tokyo, Kashiwanoha 5-1-5, Kashiwa-shi, Chiba 277-8568

¹⁰Department of Physics and Astronomy, University of Utah, Salt Lake City, UT 84112, USA

¹¹University of Oxford Astrophysics, Denys Wilkinson Building, Keble Road, Oxford OX1 3RH, UK

¹²Osservatorio Astronomico di Roma, via Frascati 33, 00040 Monteporzio (RM), Italy

¹³Australian Astronomical Observatory, PO Box 915, North Ryde NSW 1670, Australia

¹⁴Physics Department, Texas A&M University, College Station, TX 77843, USA

okumura@kustastro.kyoto-u.ac.jp

(Received ; accepted)

Abstract

We present measurements of the rates of high-redshift Type Ia supernovae derived from the Subaru/XMM-Newton Deep Survey (SXDS). We carried out repeat deep imaging observations with Suprime-Cam on the Subaru Telescope, and detected 1040 variable objects over 0.918 deg^2 in the Subaru/XMM-Newton Deep Field. From the imaging observations, light curves in the observed i' -band are constructed for all objects, and we fit the observed light curves with template light curves. Out of the 1040 variable objects detected by the SXDS, 39 objects over the redshift range $0.2 < z < 1.4$ are classified as Type Ia supernovae using the light curves. These are among the most distant SN Ia rate measurements to date. We find that the Type Ia supernova rate increase up to $z \sim 0.8$ and may then flatten at higher redshift. The rates can be fitted by a simple power law, $r_V(z) = r_0(1+z)^\alpha$ with $r_0 = 0.20^{+0.52}_{-0.16}(\text{stat.})^{+0.26}_{-0.07}(\text{syst.}) \times 10^{-4} \text{ yr}^{-1} \text{ Mpc}^{-3}$, and $\alpha = 2.04^{+1.84}_{-1.96}(\text{stat.})^{+2.11}_{-0.86}(\text{syst.})$.

Key words: supernova Ia — rate — SXDS

1. Introduction

Type Ia supernovae (SNe Ia) are remarkable objects as cosmological distance indicators, having provided the first direct evidence of the accelerating cosmic expansion. This cosmic acceleration was first reported by two independent supernova observation teams: the Supernova Cosmology Project (SCP) (Perlmutter et al. 1999) and the High-Z SN Search Team (Riess et al. 1998). Since then, many large SN surveys have been carried out to accurately measure the cosmological parameters (e.g., Knop et al. 2003; Tonry et al. 2003; Astier et al. 2006; Riess et al. 2007; Wood-Vasey et al. 2007; Kowalski et al. 2008; Hicken et al. 2009; Amanullah et al. 2010; Sullivan et al. 2011; Suzuki et al. 2012).

Although SNe Ia are effective as standard candles, their progenitors are yet to be conclusively identified. It is widely believed that the progenitor of a SN Ia is a binary system con-

taining a C+O white dwarf, and recently the compact nature of the exploding star has been confirmed (Nugent et al. 2011; Bloom et al. 2012). There are two widely discussed scenarios for the progenitor, the single degenerate (SD) scenario and the double degenerate (DD) scenario. In the SD scenario, a C+O white dwarf accretes gas from a companion star in a binary system. Its mass increases up to the Chandrasekhar limit where it explodes as an SN Ia (e.g., Nomoto 1982; Hachisu et al. 1996; Nomoto et al. 1997). If SNe Ia from the SD scenario exist, the companion star survives in the supernova remnant after the SN Ia explosion. Various methods have been used to search for such companion stars, but to date no clear detection has been made (e.g., Ruiz-Lapuente et al. 2004; Ihara et al. 2007; Gonzalez et al. 2009; Kerzendorf et al. 2009; Schaefer & Pagnotta 2012; Li et al. 2011; Nugent et al. 2011; Bloom et al. 2012; Brown et al. 2012; Chomiuk et al. 2012; Margutti et al. 2012). Other constraints on the SD scenario had been obtained from radio observations, which showed no clear evidence of an interaction between the ejecta and the circumstellar mate-

† Deceased July 19 2010

rial (CSM) surrounding the SNe. (e.g. Panagia et al. 2006; Hancock et al. 2011; Chomiuk et al. 2012). Though these observations disfavor non-degenerate donors, some SN Ia spectra show narrow time varying and/or blue-shifted Na I D absorption features possibly associated with a SD donor star (e.g. Patat et al. 2007; Simon et al. 2009; Blondin et al. 2009; Stritzinger et al. 2010; Sternberg et al. 2011; Maguire et al. 2013). These features are also investigated in the context of DD scenario (Shen et al. 2013; Raskin & Kasen 2013).

In the DD scenario, a merger of two C+O white dwarfs with a combined mass exceeding the Chandrasekhar mass leads to an SN Ia explosion (e.g., Iben & Tutukov 1984; Webbink 1984). Searches have been carried out to detect DD binaries that could be SN Ia progenitors, but strong limits have not yet been reached due to small number statistics (e.g., Koester et al. 2005; Geier et al. 2007).

SNe Ia explode with a “delay time” between binary system formation and subsequent SN explosion. This delay time is one of the primary methods for understanding the progenitor scenario of SNe Ia. Recent comparisons of the SN Ia rate and the cosmic star formation history (e.g., Madau et al. 1998; Hopkins & Beacon 2006) have resulted in a wide range of derived delay times (e.g., Cappellaro et al. 1999; Pain et al. 2002; Tonry et al. 2003; Barris & Tonry 2006; Neill et al. 2006; Poznanski et al. 2007; Botticella et al. 2008; Dahlen et al. 2008; Dilday et al. 2008; Kuznetsova et al. 2008; Graur et al. 2011; Maoz et al. 2012; Barbary et al. 2012; Perrett et al. 2012). The delay time can be predicted theoretically from the SD scenario or the DD scenario (see Wang & Han 2012, for a review). For example, in the SD scenario, the delay time is closely related to the lifetime of the companion star (e.g. Hachisu et al. 2008). The delay time obtained from rate studies can allow us to distinguish between the two progenitor scenarios.

Many studies have derived the SN Ia delay time distribution (DTD) from observations. Totani et al. (2008), for example, measured the delay time distribution based on the stellar age estimate of each galaxy in a sample of passively evolving SXDS galaxies, finding that the time distribution could be described by a featureless power law going as $f_D(t) \propto t^{-1.08 \pm 0.15}$ over $t = 0.1 - 10$ Gyr. Other studies using different methods also show consistency with a t^{-1} trend (see Maoz & Mannucci 2012, for a review).

In this context, high-redshift SN Ia rates ($z > 1$) play an important role in investigating the DTD, especially for the short delay time regime. If SNe Ia with short delay times dominate SN Ia populations, the cosmic SN Ia rate evolution should closely trace that of the cosmic star formation, and thus high-redshift SN Ia rates provide information about the short delay time population.

High-redshift SN Ia rates have been measured in several surveys. Recently, Perrett et al. (2012) has measured the SN Ia rate over the redshift range $0.1 \leq z \leq 1.1$ using 286 spectroscopically confirmed and $\gtrsim 400$ photometrically identified SNe Ia from the Supernova Legacy Survey (SNLS). Dahlen et al. (2008; hereafter Da08) obtained the first SN Ia rate measurement beyond z of 1, based on the Great Observatories Origins Deep Survey (GOODS) survey. They used 56 high-redshift SNe Ia, the majority of which were spec-

troscopically confirmed. Interestingly, they find that the SN Ia rate decreases beyond $z \sim 1.6$, contradicting the expectation from the delay time distribution measurements of Totani et al. 2008. However, the rate in the highest redshift bin ($z \gtrsim 1.4$) has a large uncertainty due to small number statistics. The detection efficiency at $z > 1.4$ rapidly decreases with redshift as the observed bands shift farther into the rest-frame UV. Other high- z rate measurements have been reported in the literature. Graur et al. 2011 derived the SN Ia rate up to $z \sim 2.0$ using 150 SNe from a SN survey in the Subaru Deep Field (SDF), and found that the SN Ia rate levels off at $1.0 < z < 2.0$. Their SN classification method is based on a single epoch in the $R, i',$ and z' bands, provided in Poznanski et al. 2007. Barbary et al. 2012 (hereafter B12) derived the SN Ia rate up to $z \sim 1.6$ using ~ 20 SNe Ia from the *Hubble Space Telescope* Cluster Supernova Survey, finding a rate that is broadly consistent with previous measurements but with large uncertainties. The behavior of SN Ia rates at high redshifts is not clear yet due to the large statistical uncertainties associated with the few detections to date in this redshift range. This is a key issue in SN Ia rate studies.

In this paper, we measure the SN Ia rate to high redshift using the Subaru/XMM-Newton Deep Survey (SXDS) data set. The survey area is large ($\sim 1 \text{ deg}^2$) enough to obtain many SNe Ia. With the repeat imaging observations we are able to construct high-quality SN light curves. We obtain 39 SNe Ia in the range $0.2 \lesssim z \lesssim 1.4$ using a classification method that relies primarily on light-curve fitting and photometric redshifts. Spectroscopic identifications, source colors, host galaxy redshifts, and X-ray data are employed when available to directly remove contamination or to improve statistical contamination corrections.

The paper is organized as follows. In §2, we describe the observations. We briefly summarize the SXDS data set, and describe in detail the observations used for SN detection. In §3, we describe the SN selection method. In §4, we describe the control time calculation. In §5, we discuss the results and estimate systematic errors. We provide Figure 1 as a visual guide to the procedure used in this paper. In §6, we compare our results with previous works. Finally, we summarize our work in §7. Throughout the paper we adopt the cosmological parameters $H_0 = 70 \text{ km s}^{-1} \text{ Mpc}^{-1}$, $\Omega_M = 0.3$, $\Omega_\Lambda = 0.7$. All magnitudes are given in the AB system.

2. Observations

2.1. Imaging observations

The Subaru/XMM-Newton Deep Survey (SXDS) is a multi-wavelength survey from X-ray to radio (Sekiguchi et al. 2004). The survey targets a 1.22 deg^2 field centered on $(02^{\text{h}}18^{\text{m}}00^{\text{s}}, -05^{\circ}00'00'')$, hereafter referred to as the Subaru/XMM-Newton Deep Field (SXDF). The optical imaging component of the survey was carried out using Suprime-Cam (Miyazaki et al. 2002) on the 8.2-m Subaru telescope, starting in September 2002. With Suprime-Cam’s very wide field of view ($34' \times 27'$), the field is covered in five pointings (SXDF-C, SXDF-N, SXDF-S, SXDF-E and SXDF-W; see Furusawa et al. 2008). In order to detect and follow the light

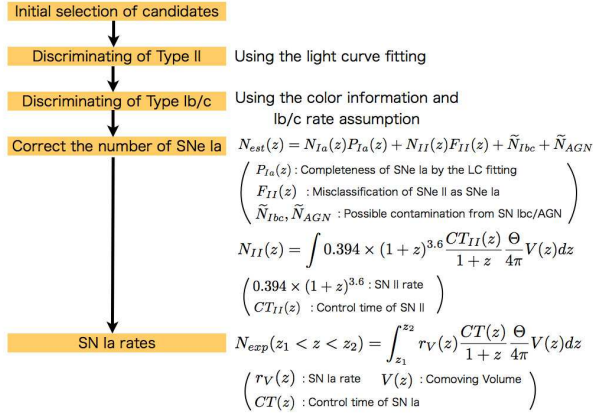


Fig. 1. The flow chart of the rate calculation. Since the SN classification has a bias, we need to correct the number of SNe Ia identified by their light curves using artificial light curves made by the Monte Carlo simulations.

curves of optically faint variable objects, the Suprime-Cam observations were split into exposures of 1800–7200 seconds separated by periods of days to weeks. Between September 2002 and December 2002, the fields were observed 5–7 times in the i' -band and 2–4 times in the R_c - and z' -bands. After the 2002 observations finished, we took reference images in the i' -band in 2003 and 2005, in the z' -band in 2005, and in the R_c -band in 2008. The observations are described in detail in Morokuma et al. (2008a, hereafter M08). Here, the number of the epochs of the observations, each exposure time, and each detection limit are summarized in Table 1. For our SN study we exclude regions around bright objects to ensure reliable detection of object variability. This reduces the total effective area to 0.918 deg^2 .

X-ray imaging observations in the SXDF were carried out with the European Photon Imaging Camera (EPIC) on the XMM-Newton. The X-ray imaging covers most of the SXDF fields. The X-ray observation details are described in Ueda et al. (2008) and Akiyama et al. (in preparation). The limiting fluxes are to $1 \times 10^{-15} \text{ erg cm}^{-2} \text{ s}^{-1}$ in the soft band (0.5–2.0 keV) and $3 \times 10^{-15} \text{ erg cm}^{-2} \text{ s}^{-1}$ in the hard band (2.0–10.0 keV).

2.2. Spectroscopic observations

Follow-up spectroscopic observations to identify transients and obtain redshifts were taken during the survey in 2002. The follow-up was done with several ground-based 8–10m telescopes and the ACS grism on HST and is described in Lidman et al. (2005), Morokuma et al. (2010) and Suzuki et al. (2012). Given the large number of transients, priority was given to transients that were likely to be SNe Ia at $z > 1$. A number of factors went into computing the priority: the significance of the detection, the percentage increase in the brightness, the distance from the centre of the apparent host, the brightness of the candidate and the quality of the subtraction (the follow-up procedure is summarized in Lidman et al. 2005). In total, 8 transients, half of which are beyond $z = 1$, were classified as SN Ia (see Table 3 for the references). In

later years, additional spectroscopic observations were taken with FOCAS on Subaru to obtain redshifts of host galaxies after the transients had faded from view.

3. SN selection

In order to obtain a sample of SNe Ia we have selected variable objects from our multi-epoch data and then applied a series of procedures to further purify the sample. The first such procedure consists of lightcurve fitting to reject objects whose lightcurves are inconsistent with an SN Ia. This procedure can be applied to all candidates. Additional procedures make use of color, spectroscopic and additional information available for subsamples of the full sample to further cull the sample. These procedures are now described in detail.

3.1. Variability selection

The details of the initial selection of variable objects in the SXDF are described in detail by M08. In brief, we use an imaging subtraction method introduced by Alard & Lupton (1998) and developed by Alard (2000), which enables us to match one image against another image with a different PSF. We can then detect and measure variable objects in the subtracted images. This method is applied for all possible pairs of stacked images at different epochs. In the subtracted images, we select objects having a flux greater than $5\sigma_b$ in an aperture of 2 arcsecond in diameter, where σ_b is the background fluctuation within an aperture of this size. A total of 1040 variable objects were detected. We are selecting supernovae that occurred in 2002; since supernovae light curves last only a few months, there should be no variability detected in 2003 or 2005. Of 1040 variable objects, only 371 did not show variability (above $5\sigma_b$) in 2003 and 2005. These 371 objects are classified as transients. For computing light curves, we then assume that there is no flux from the transient in images taken from 2003 onwards. Finally, we require that objects show at least a $5\sigma_b$ increase in 2 or more epochs in the i' -band. If a variable object is only detected in one epoch, the object might be a false detection due to galaxy missubtraction, or another kind of transient phenomenon. Note that this requirement is accounted for in the rate calculation during the calculation of the control time (§4.1).

We applied one further consideration at this stage; at redshift $z \sim 1.4$, the central wavelength of the SuprimeCam i' band corresponds a rest-frame wavelength of $\sim 3250\text{\AA}$. The properties of supernovae, of all types, are not well characterized over this wavelength region, limiting the effectiveness of non-spectroscopic classification methods. For this reason we remove 5 objects whose spectroscopic redshift are $z > 1.4$. However, we also note that it is still possible to detect a SN Ia with $z > 1.4$ (see §3.1.2 for a possible candidate). After this stage, 141 variable objects remain as SN candidates.

3.1.1. Host galaxy redshifts

Although we would need spectra of both host galaxies and supernovae in order to identify host galaxies with absolute certainty, here we simply identify the galaxy closest on the sky to each SN candidate as its host (M08). The stacked images of

SXDF are much deeper than the individual images, which enables us to detect a reliable host galaxy for every SN candidate. Of the 141 host galaxies, only 22 have a spectroscopic redshift. Redshifts for the SN host galaxies without spectroscopic redshifts are derived from photometric redshifts of the host galaxies using the multi-color photometric dataset of SXDS. The stacked images from the Suprime-Cam observations have depths of $B = 28.4$, $V = 27.8$, $R_c = 27.7$, $i' = 27.7$, and $z' = 26.6$ (3σ , 2 arcsecond diameter aperture; Furusawa et al. 2008). As part of the SXDS, the field was observed by the UKIDSS/UDS survey (Warren et al. 2007) in the J, H, and K bands, with respective limiting magnitudes of 24.9, 24.2, 24.6 (5σ , 2 arcsecond diameter aperture). Additionally, the SWIRE survey (Lonsdale et al. 2004) obtained data in 3.6 μm and 4.5 μm bands, with respective limiting magnitudes of 23.1 and 22.4 (3σ , 3.8 arcsecond diameter aperture).

Photometric redshifts are calculated using this 10 band dataset. Photometric redshift calculations are performed using the publicly available code *LePhare* (Arnouts et al. 1999; Ilbert et al. 2006). We fit our B , V , R_c , i' , z' , J , H , K , 3.6 μm , 4.5 μm host magnitudes with spectral energy distributions (SEDs) from PEGASE2 (Fioc & Rocca-Volmerange 1997, 1999) stellar population synthesis models. We use the initial mass function of Scalo (1986) and 15 models for star formation (SF) history. These include a constant star formation rate (SFR) scenario, starburst scenario, and star formation history having an exponentially decaying SFR with exponential time scales of $\tau_{\text{SF}} = 0.1, 0.3, 0.5, 0.7, 1, 2, 3, 5, 7, 9, 10, 15$, and 20 Gyrs.

To test the reliability of the photometric redshifts (z_{ph}), we use 786 SXDS galaxies that have both a photometric redshift and a spectroscopic one. The comparison is shown in Figure 2. The reliability depends on the redshift range and the uncertainty of the host-galaxy photometry. Most galaxies ($\gtrsim 80\%$) are in the range $-0.1 < (z_{sp} - z_{ph})/z_{ph} < 0.2$. Since our work concentrates on the determination of SN Ia redshifts, we use the probability distribution function (PDF) of the host galaxy redshift when classifying its type and redshift.

It is possible that some host associations are erroneous, which could result in the rejection of a bona fide SN Ia due to an error in the lightcurve timescale. An erroneous association between objects with similar redshifts — such as those in the same group or cluster — is not of concern here. To check for possible host galaxy misidentification, for the objects which we later classify as SN Ia we show in Figure 7 the distribution of separations between the SN and the center of its designated host galaxy. According to Yasuda & Fukugita (2010), the radial distribution of SNe Ia is nearly consistent with the luminosity profiles of their host galaxies. In the case of our SXDS candidates, a Kolmogorov-Smirnov test finds the distribution of the SN Ia candidates to be consistent with the luminosity profiles of galaxies (Yasuda & Fukugita 2010). Therefore, we assume that erroneous host associations are unimportant for the present analysis.

3.1.2. Discriminating Type II SNe

The light curves of SNe II are generally significantly broader than those of SNe Ia or SNe Ib/c. Therefore, as a first step we distinguish between SNe I (including Ia, Ib and Ic) and SNe II

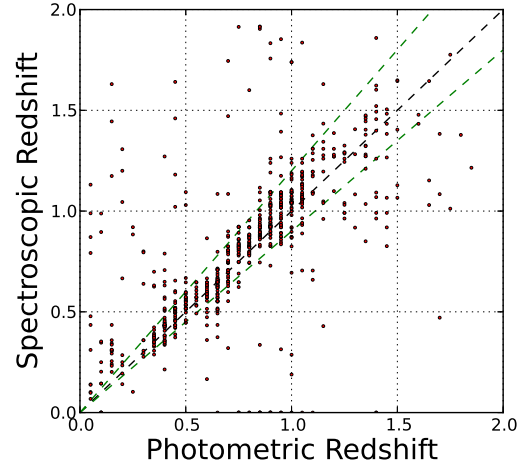


Fig. 2. Spectroscopic redshifts (z_{sp}) versus photometric redshifts (z_{ph}) of SXDS galaxies. The green dashed lines indicate the region bounding $-0.1 < (z_{sp} - z_{ph})/z_{ph} < 0.2$.

using the light-curve shape. To do this, we compare the light curve of each candidate to template light curves of the various SN subtypes. As we will see, the light curves of most candidates are adequately sampled to distinguish unambiguously between SNe I and SNe II. Where available, we use the spectroscopic redshift of the SN or host galaxy in the light-curve fitting. Where there is only a photometric redshift available, we use the PDF of the host galaxy calculated by *LePhare* as a redshift prior.

We construct SN Ia and SN II template light curves in the observed i' -band using K -corrections derived from the spectral time-series templates of Hsiao et al. (2007) and Nugent et al. (2002). The shape of various SN Ia light curves can be well-represented by a single template and a stretch factor (Perlmutter et al. 1997). For the SN Ia light curves we perform K -corrections with the spectral template of Hsiao et al. (2007). This template accurately describes the UV features of SNe Ia, which is particularly important for high-redshift SNe Ia. SN Ia light-curve shape diversity can be neglected as it has been shown to be small compared to the difference between SNe Ia and SNe II light-curve shapes (Takanashi et al. 2008). In contrast to SNe Ia, it is impossible to describe SNe II with only one template. Type II SNe can be divided into several subtypes (e.g., IIP, IIL and IIIn) each of which exhibits a broadly different light-curve shape. Even within subtypes there is significant light-curve shape diversity. Therefore, we use a set of 12 well-observed SN II light curves as templates. Our observed SNe II consist of 5 of the best-observed published SNe II and 7 SNe II from the SDSS-II SN survey (Sako et al. 2008). In total, the SDSS-II SN survey observed more than 50 SNe II over three years. The 7 used here are selected based on their discovery at an early phase and many repeat observations (> 10) with long time coverage (~ 60 days) in the SDSS u' -, g' -, and r' -bands. Details for the 12 SNe II used as templates are listed in Table 2. For each candidate, an i' -band template light curve is made by K -correcting the observed multi-band photometry to the redshift of the candidate, using the templates

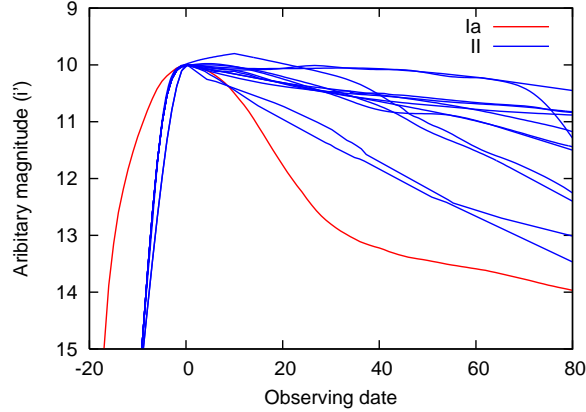


Fig. 3. Examples of light curve templates in the observed i' -band: A single SN Ia template at $z = 0.9$ (red line) and 12 SN II templates at $z = 0.5$ (blue lines) are shown.

of Nugent et al. (2002). Generally, the observed SN II light curves lack data points during their rising phase due to the rapid increase to maximum after explosion. Thus, we also use the Nugent et al. (2002) templates to interpolate the rising phase of the light curve. Example template light curves for Type Ia and II SNe are shown in Figure 3.

Using the observed i' -band light curve of each SXDS SN candidate, we perform the following fitting method to refine candidates.

First, we use the probability of being a certain type of SN as a function of redshift using the following formula:

$$P_{\text{type}}(z) \propto \text{PDF}(z) \times \exp \left\{ -\frac{\chi_{\text{LC}}^2(z)}{2} \right\} \quad (1)$$

Here, $\text{PDF}(z)$ is the probability function derived by *LePhare*, and χ_{LC}^2 is the χ^2 calculated by light curve (LC) fitting.

$$\chi_{\text{LC}}^2(z) = \sum_{k=1}^n \left\{ \frac{f_{\text{obs}} - f_{\text{temp}}(z)}{\Delta f_{\text{obs}}} \right\}^2, \quad (2)$$

where f_{obs} is the observed i' -band flux, Δf_{obs} is the observational error, $f_{\text{temp}}(z)$ is the i' -band flux of the template light curve at redshift z , and n is the number of observing epochs during 2002: 7 in SXDF-C and SXDF-W, 6 in SXDF-E, and 5 in SXDF-N and SXDF-S. Note that $f_{\text{temp}}(z)$ represents a set of templates of SNe of different types. In the light-curve fit, the free parameters on the template light curve are the peak magnitude, the date at peak brightness, the stretch factor, and the redshift. Then we calculate the value of χ_{LC}^2 for each SN template. The date at peak brightness is allowed to vary between day -10 and 70 where day 0 corresponds to the beginning date of the SXDS variable object survey (September 30, 2002). The stretch factor is only used in fitting the Type Ia template. It is constrained to the range $0.75 - 1.2$ and moves independently of peak magnitude. For SNe Ia templates, the B -band absolute magnitude is allowed to vary in the range $-20.0 < M_B < -17.0$. This magnitude range is based on the range of the real SN Ia distribution observed in the SDSS-II SN survey (Dilday et al. 2008). For SNe II templates, the V -band absolute magnitude is allowed to vary in the range

$-19.0 < M_V < -15.0$. As for SNe Ia, this range is based on the distribution of SNe II in the SDSS-II SN survey (see Figure 9). In all cases, the absolute magnitude is converted to an observed i' -band magnitude using the luminosity distance and a K -correction with the appropriate spectral template (Hsiao et al. 2007 and Nugent et al. 2002). For SNe having spectroscopic redshifts, the redshift is fixed, and f_{temp} is calculated by K -correcting the light-curve template to that redshift.

We determine the SN type by inspecting the value of $P_{\text{type}}(z)$. If the $P_{\text{type}}(z)$ obtained by fitting the SN Ia template is greater than that obtained by fitting any of the SN II templates, the candidate is classified as a SN I. In order to remove candidates that are neither SNe I nor II (i.e., AGN or other variable objects), we also require that the $\chi^2/d.o.f.$ for the best fit template be lower than 5. Based on the simulation of completeness (§4.2), 98.4% of real SNe Ia will satisfy this requirement.

Using this method, we classify 44 of the 141 candidates as SNe I. Though our control time shows a sharp drop off by $z \sim 1.4$, one object (1-081) has been classified as SN Ia at $z = 1.45$ with $M_B = -19.53$. It is possible to detect a SN Ia with $z > 1.4$ if our observations cover at least two epochs around the maximum (see Figure 10). However, we do not include this object in the rate calculation and use only the 43 SNe I having $z < 1.4$. Examples of template light-curve fits are shown in Figure 4. Although we expect this method to distinguish between SNe I and II with good reliability (see following section), due to statistical fluctuations the classification will not be perfect. Therefore, we estimate and correct for completeness and SN II contamination in §4.2.

3.1.3. Discriminating against AGN

Another potential source of contamination are AGN that pass our variability cuts. X-ray detection is useful in confirming whether or not variable objects are AGN. Out of 43 SN Ia candidates, 42 objects were observed with XMM-Newton at some observation phase of SXDS, and only two object are detected in X-ray. This X-ray detection ratio is almost the same as the ratio of AGN to general galaxies (M08). Thus, the one object detected in X-ray might be supernova that occurred in a galaxy hosting an AGN.

We have a spectrum of one of the transients associated with an X-ray source, object 3-202 (SuF02-061). The spectrum exhibits an [Ne III] $\lambda\lambda 3869$ emission line, suggesting the possibility of an AGN. [O II] $\lambda\lambda 3727$ and $H\delta$ are also detected. From these lines, we derive [Ne III]/ $H\delta \sim 0.35$ and [O II]/ $H\delta \sim 0.61$, which are consistent with either an AGN or starburst origin (Rola et al. 1997, Pérez-Montero 2007).

Tests performed on the spectrum indicate that, had object 3-202 been a SN Ia, we would have detected the SN Ia features. Object 3-202 is also very close to the core of its host galaxy, as expected for an AGN. The offset is 0.19 pixels ($0''.04$), which is larger than our expected measurement uncertainty. Thus, while we are unable to rule out the possibility of a SN Ib/c associated with a starburst, with this evidence we can conclusively reject the possibility that this object is a Type Ia SN.

We also reject object 1-143, due to the likelihood that it is an AGN. Unlike 3-202, we do not have a spectrum of object

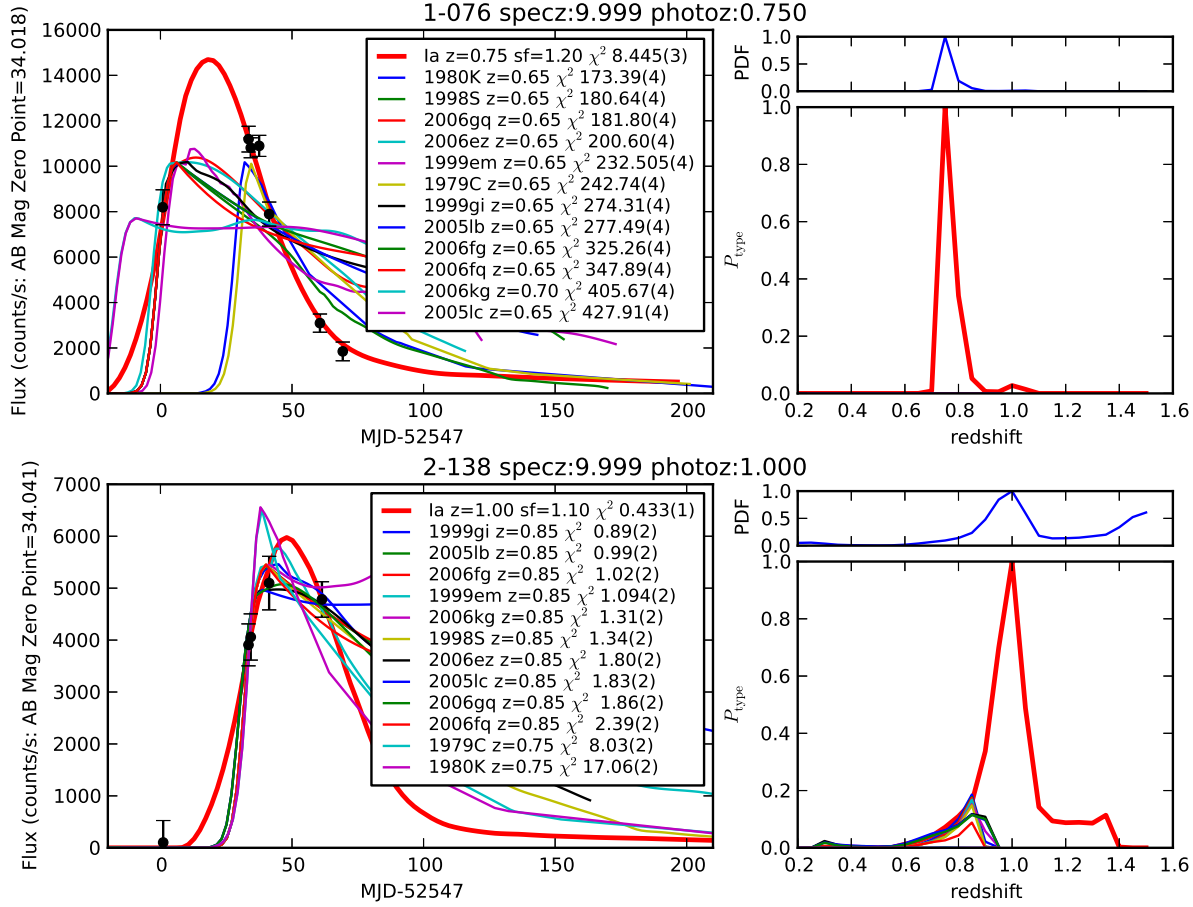


Fig. 4. Two examples demonstrating the method we use to classify SNe. On the left, we show the best fits using the templates used in this paper. The numbers in the parenthesis are reduced χ^2 values. The right-hand plots show the PDFs of the host galaxies and the normalized P_{type} as a function of redshift. The best fit for the object in the upper panels is a SN Ia at $z = 0.75$. This is a typical case. The object in the lower panels is an example of an object that has a type that is less clear. Though this object is best fit with a SN Ia template, the P_{type} distribution shows that SNe II are possible. However, the signature of SN Ia is still strong here and the object is classified as a SN Ia in our sample. The possible contamination of SN II from the fitting is taken into account (see §4).

1-143; however, it is detected in the X-rays and is closer to the core of its host galaxy than any other candidate.

X-ray observations are usually powerful tools to detect AGN, however not all AGN have X-ray detections and faint AGN populations are not traced by X-ray observations (M08). Since objects 3-202 and 1-143 passed the lightcurve test but are likely AGN, we may ask whether there are other such cases of AGN undetected by X-rays in our sample. Only one other object, 4-203, is as close to the core of its host as objects 3-202 and 1-143 are to theirs. If this was an AGN as well, our sample would have a deficit in the number of SNe Ia near core, so we deem it likely that this object is not an AGN.

3.1.4. Discriminating against Type Ib/c SNe

At this point we have 41 SN Ia candidates based on their light-curve shapes. It is impossible to further classify candidates into SNe Ia and Ib/c without additional data because the shapes of SN Ia and Ib/c light curves are quite similar. Although SNe Ib/c are rarer events than SNe Ia, we expect that the classified SNe I will include a few SNe Ib/c.

In our observation, some transients were observed in R_c —

and z' —bands. We make use of this photometry to discriminate SNe Ib/c from SNe Ia based on color information ($R_c - i'$ vs $i' - z'$); 14 of the remaining SNe I candidates have this color information. The AGN 3-202 also has a color measurement, as do 2 of the 8 spectroscopically-confirmed SNe Ia. We construct color-color diagrams of the candidates at each redshift and epoch where the colors are available (Figure 5). The color models of SNe Ia and Ib/c are obtained from the templates of Hsiao et al. (2007) and Nugent et al. (2002), respectively. We assume an average reddening from SN host galaxies and show the reddening as arrows on Figure 5. SN Ia candidates are grouped by similar redshift and epoch so that we can compare the expected SN Ia/Ibc colors and those of candidates.

Using Figure 5, we estimate that 2 out of the 14 remaining candidates have a color incompatible with SNe Ia. These objects, 2-038 and 4-100, are therefore rejected from the sample. Possible contamination of SN Ib/c on the rest of the sample is discussed in §4.2.3 as a systematic uncertainties.

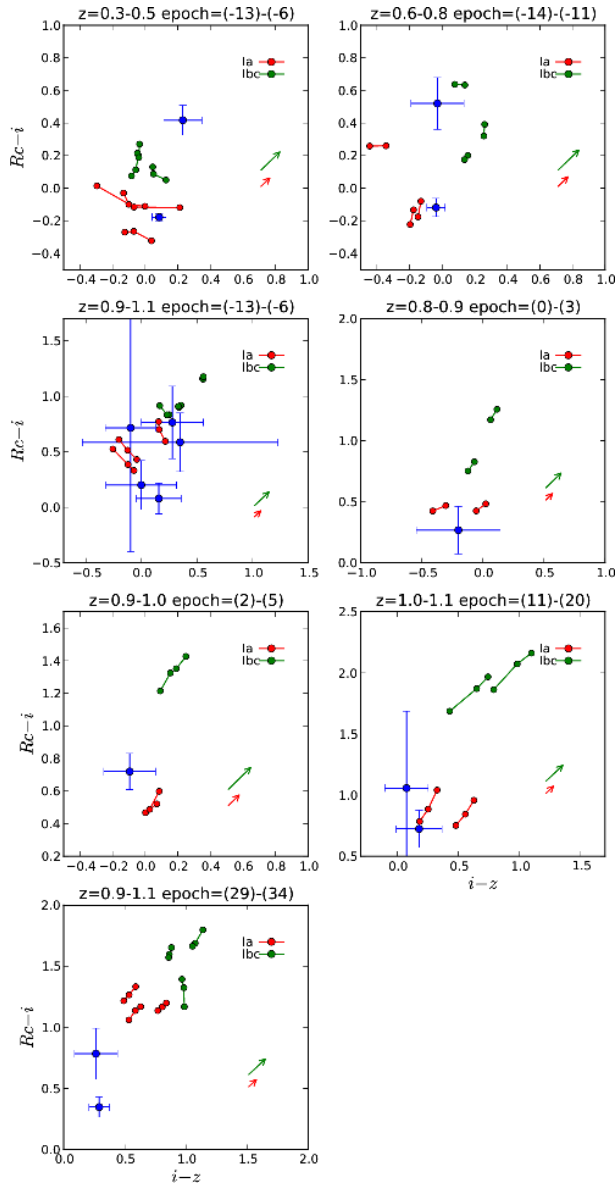


Fig. 5. The color-color diagrams of SN I candidates in the observer frame. The red lines and green lines indicate the expected colors of unreddened SNe Ia and SNe Ib/c respectively at the given redshift. The points connected by the lines indicate the values at specific epochs in the epoch range given. Red and green arrows indicate average reddening of supernovae from their host galaxies: $A_B = 0.4$ for SNe Ia (Wang et al. 2006) and $A_B = 0.7$ for SNe Ib/c (Richardson et al. 2006). Blue circles show the colors of the SN I candidates in SXDS. Out of 15 candidates, two candidates have colors most similar to SNe Ib/c.

3.1.5. Properties of SN Ia candidates

We can use the small subset of the candidates that are spectroscopically confirmed SNe Ia as a basic consistency check. All 8 spectroscopically confirmed SNe Ia and probable SNe Ia (Ia*) found during the SXDS are classified as SNe I by the light-curve fitting.

Although the 39 SN Ia candidates will have some contamination from SNe II (estimated in §4.2) and SNe Ib/c (§4.2.3), we expect most of them to be SNe Ia. We can check that most of the 39 SN I candidates have properties broadly consistent with SNe Ia. The best fit light-curve parameters for each of the 39 candidates are shown in Table 3. We note that the uncertainty in these parameters is often large, particularly for candidates lacking a spectroscopic redshift. This is not a problem however, as we are concerned with the broad light-curve characteristics of the sample as a whole rather than an precise determination of the light-curve parameters of any single SN. We discuss the distribution of absolute magnitude, light-curve width, and host galaxy separation for the candidates.

Absolute magnitude. The distribution of the candidates' B-band absolute magnitudes (uncorrected for host galaxy extinction) is shown in Figure 6 (top). The distribution peaks around $M_B \sim -19.0$, the expected average magnitude of SNe Ia. The expected distribution of SN Ia magnitudes from this survey (based on the simulations described in §4) is shown as a dotted line. There appears to be an overabundance of faint candidates, possibly due to contamination from SNe II. The lower panel of Figure 6 shows where the excess lies in redshift – the excess faint candidates are found mainly at lower redshift ($z < 0.8$). Note that the simulated expected distribution (green contours) takes into account the shift in the distribution of SNe toward higher luminosity and larger stretch with redshift (e.g., Howell et al. 2007). As a result, the top of the green contours slopes up with redshift.

Light curve width. Since our light curve fitting is based on at most seven epochs, constraining the light curve width (stretch parameter) is challenging compared to other parameters, e.g., M_B , and the day of maximum. Their errors are very large ($\Delta s \sim 0.1 - 0.2$). Furthermore, our stretch factors in Table 3 are not B-band stretch factors but observed i' -band stretch factors, which correspond to other rest-frame bands depending on redshift. This is not a problem here, however, since we are employing light curve fitting only to determine type and redshift. The observer-frame i' -band stretch distribution contains a broad peak around $s \sim 1$, which is consistent with observations of nearby SNe Ia. At the same time, we found that some faint objects have large stretches ($s \sim 1.2$), though we expect large stretches for luminous objects. Some of these objects might be misclassified SNe II. We estimate the rate of misclassified SNe II in §4.2.2.

Host galaxy separation. We show the distribution of the distance from each candidate to the center of its designed host galaxy (Figure 7). According to Yasuda & Fukugita (2010), the radial distribution of SNe Ia is nearly consistent with the luminosity profiles of their host galaxies. In the case of our SXDS candidates, a Kolmogorov-Smirnov test finds the distribution of the SN I candidates to be consistent with the luminosity profiles of galaxies.

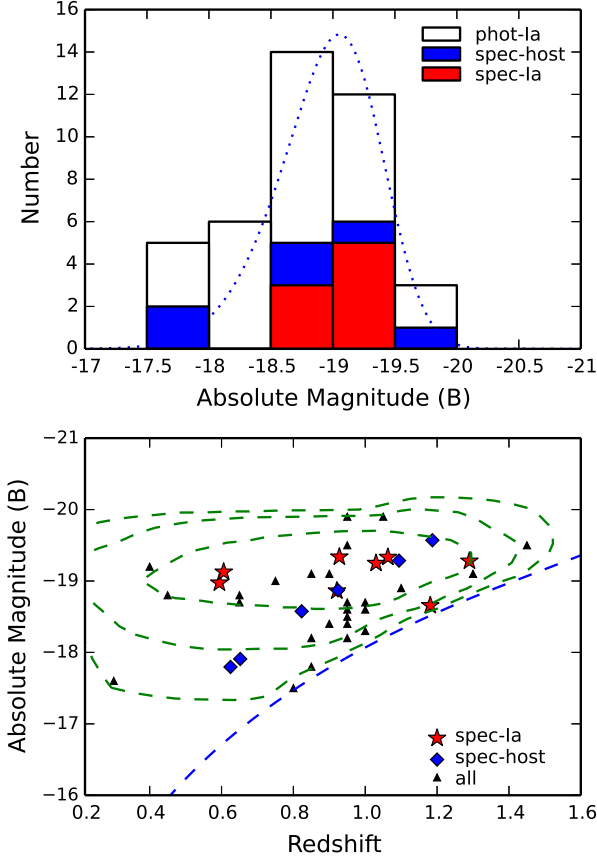


Fig. 6. The observed peak magnitude distribution of SNe Ia candidates in our SXDF sample. The *top figure* shows the number distribution. Spectroscopically-confirmed SN Ia, not spectroscopically-confirmed SN Ia but objects with spectroscopic redshifts from host galaxies, and other SN Ia candidates are plotted as red, blue and open histograms, respectively. The *bottom figure* shows the redshift distribution of the SN Ia candidates. In the bottom figure, the *red stars* describe the SNe Ia SNe confirmed by spectroscopic observations, the *blue diamonds* describe the candidates with spectroscopic redshifts from their host galaxies, and the *black triangles* describe the remaining SN Ia candidates. The *blue dotted line* describes the limiting magnitude of the SXDS observations. The *green contours* show the 1-, 2- and 3- σ confidence intervals for the distribution of a pure SN Ia sample calculated using the methods and SN rates from §4.

3.1.6. The estimated number of observed SN Ia

To count the estimated number of observed SNe Ia (N_{est}), the easiest way might be to use the best-fit redshift derived from the fitting. However, some SN Ia candidates have large host photo- z uncertainties (see bottom right figure of Fig. 4 for an example). Instead, we allocate the number of SN Ia according to their P_{type} distributions. For example, in the case of 2-138 illustrated in Fig. 4, we allocate a fractional contribution of 0.55 to the $0.6 < z < 1.0$ bin and 0.45 to the $1.0 < z < 1.4$ bin. These allocations are summarized in Table 3, where it can be seen that the probability is concentrated in a single bin for each SN.

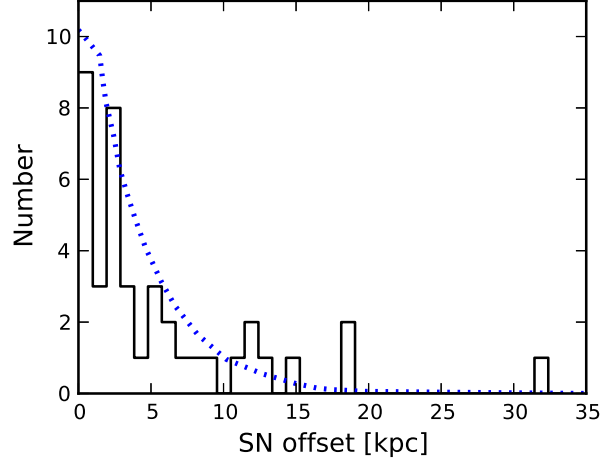


Fig. 7. The distribution of distance between candidate and host galaxy center for the SN I candidates. The *black solid line* indicates the distribution of SN I candidates and the *blue dotted line* indicates the luminosity profiles of galaxies (Yasuda & Fukugita 2010).

4. Rate Calculation

Given the supernova rate per unit comoving volume $r_V(z)$, the average number of SNe we expect to observe in the redshift bin $[z_1, z_2]$ is given by

$$N_{exp}(z_1 < z < z_2) = \int_{z_1}^{z_2} r_V(z) \frac{CT(z)}{1+z} \frac{\Theta}{4\pi} V(z) dz, \quad (3)$$

where $V(z)dz$ is the comoving volume in a redshift slice of width dz , Θ is the solid angle observed in the survey (in units of steradians), and $CT(z)$ is the observer frame “control time”. The control time can be thought of as an “effective visibility time”; it is the total time (in the observer frame) for which the survey is sensitive to a SN Ia at redshift z . In any survey of finite length, the observed number of SNe in any given bin will differ from the average expected number N_{exp} due to Poisson statistics. Given a functional form of the rate $r_V(z)$, we can estimate its parameters by comparing the observed number of SNe to N_{exp} in each redshift bin. Alternatively, we can make the approximation that the rate is constant within each bin. Under this approximation, $r_V(z)$ can be moved outside the integral in equation (3). Using N_{Ia} as an unbiased estimator of N_{exp} , we get an estimate of the rate in the bin $z_1 < z < z_2$,

$$\hat{r}_v(z_1 < z < z_2) = \frac{N_{Ia}(z_1 < z < z_2)}{\int_{z_1}^{z_2} \frac{CT(z)}{1+z} \frac{\Theta}{4\pi} V(z) dz}. \quad (4)$$

Since $CT(z)$ differs by changing position (field) and survey epochs, $CT(z)$ is calculated for all fields and corresponding survey parameters, then normalized for the rate calculations. In this paper, we use two methods. Assuming the rate follows a simple power law, $r_V(z) = r_0(1+z)^\alpha$ (Pain et al. 2002), we estimate its parameters using equation (3). We also use equation (4) to estimate the rate in three broad bins, $0.2 < z < 0.6$, $0.6 < z < 1.0$, $1.0 < z < 1.4$.

Because we have a spectroscopic classification for only a small minority of our SN candidates, we use a photometric typing method as our primary means of classifying into SNe I and

II, thereby arriving at an estimated number of SNe Ia observed, N_{est} . This method can give a biased estimate of the true number of SNe Ia, N_{Ia} , due to the limited number and precision of observations. Specifically, some Type II SNe may be misclassified as SNe Ia, while some Type Ia SNe may be misclassified as SNe II. The estimated number of SNe Ia, N_{est} , can be expressed as follows:

$$N_{est}(z) = N_{Ia}(z)P_{Ia}(z) + N_{II}(z)F_{II} + \tilde{N}_{Ib/c} + \tilde{N}_{AGN}, \quad (5)$$

where P_{Ia} is the probability of correctly classifying a SN Ia (completeness) and F_{II} is the probability of classifying a SN II as a SN Ia (contamination). Note that these two factors address only misclassification in the light-curve fitting, not uncertainties in the SN Ia or II light-curve templates. Those uncertainties are addressed in our estimate of the systematic error (§5). $\tilde{N}_{Ib/c}$ and \tilde{N}_{AGN} are possible residual contamination from SN Ib/c and AGN, as described in §3.1.3 and §3.1.4. The method we use to derive the rates is illustrated in Figure 1. In §4.1 we calculate $CT(z)$ using simulated SN Ia light curves. In Section §4.2 we calculate $P_{Ia}(z)$ and $F_{II}(z)$ using simulated SN Ia and II light curves. The number of SNe II, $N_{II}(z)$, is calculated assuming the nearby SN II rate and cosmic star formation history.

4.1. Control time

The control time is the time interval during which we can detect the SN explosion. Here we define the time in the observer-frame. We compute the control time as a function of redshift.

4.1.1. Simulated light curves of Ia and II

In order to calculate the control time, we carry out a Monte Carlo simulation to generate artificial “observed” SN Ia and SN II light curves based on the observation dates and depths of our SXDS variable object survey. To produce a distribution of artificial SNe Ia modeled on the true SN Ia distribution, we use a magnitude distribution based on SNe Ia from the SDSS-II SN survey (Frieman et al. 2008). As the SDSS-II sample is essentially complete at $z \leq 0.12$ (Dilday et al. 2008), we adopt the exact absolute magnitudes and stretch factors of 56 $z \leq 0.12$ SDSS-II SNe for our artificial SNe Ia. The 56 SNe include all spectroscopically-confirmed $z \leq 0.12$ SNe Ia obtained in the first two years (2005 and 2006) of the survey. The B -band absolute magnitude distribution (uncorrected for dust extinction) and B -band stretch factor distribution of these SNe Ia is shown in Figure 8. The stretch distribution of SNe Ia at high-redshift might be different from the local distribution; according to Howell et al. (2007) the average light curve width and average intrinsic luminosity of SNe Ia increase toward high-redshift for non-subluminous SNe Ia. Therefore we include the effect of the stretch evolution toward high-redshift in our simulation. At each redshift, we make an artificial light curve in the observed i' -band based on each of the 56 SNe. To do this, we use the absolute magnitude of the SN and a K -correction based on the $u'g'r'i'$ SDSS-II light curve and the Hsiao et al. (2007) template. Though we use real SNe Ia, including what-

ever dust extinction they suffer, for our control time simulation in order to represent the actual $M_B - s$ distribution, an alternative approach is to employ a simple parameterized family of lightcurves, e.g., using stretch and color, c . B12 simulated the magnitude distribution of SNe Ia using the model:

$$M_B = -19.31 - \alpha(s - 1) + \beta c + I \quad (6)$$

where -19.31 is the fiducial magnitude, $\alpha = 1.24$, $\beta = 2.28$ (Kowalski et al. 2008), and I is an additional “intrinsic dispersion” characterized with $\mu = 0.0$ mag and $\sigma = 0.15$ gaussian distribution. The top panel of Figure 8 shows the comparison between simulated magnitude distributions for dust models from B12 and that of our sample. Our sample is well represented by the distribution with the extinction model presented in Kessler et al. 2009 (hereafter K09), which is expressed as $P(A_V) \propto \exp(-A_V/0.33)$ from host-galaxy SN extinction in the SDSS-II SN Survey. Among the models examined in B12, the model of Hatano et al. (1998), which was used for the main result in Dahlen et al. (2008), was the most dust-affected model. This model is also indicated in the top panel of Figure 8, showing tail to the fainter side. The uncertainty caused by the choice of extinction models is discussed in §5.

Next, we make artificial SN II light curves from the Type II templates of §3.1.2. As for SNe Ia, the absolute magnitude distribution for these light curves is based on real SDSS-II SNe. However, it is more difficult to achieve a complete sample for SNe II because they are intrinsically fainter than SNe Ia on average. If we use the same redshift cut off as for SNe Ia ($z = 0.12$), the number of faint SNe II will be underestimated (see Figure 9). To resolve this problem, we have constructed a new luminosity function that accounts for incompleteness using the formula below:

$$N_{eff}(L)dL = N_{sdss}(L)dL \times \frac{V_{z < 0.17}}{V_{z_{max}|L}} \quad (7)$$

where $N_{SDSS}(L)dL$ is the number of SDSS SNe II with luminosity $L - \frac{dL}{2} < L < L + \frac{dL}{2}$ and $V_{z_{max}|L}$ is the volume to which a SN II can be seen above the SDSS flux limit given the luminosity, L . Thus, we can simulate lightcurves using essentially all of the real SNe II from SDSS-II. We will estimate the systematic error due to the correction factors in §5 by varying the SDSS flux limit. In addition to a distribution in absolute magnitude, we use two different subtypes (Type IIP and IIL) in our generated artificial SN II light curves. We use a ratio of Type II-P to Type II-L of 2:1 (Richardson et al. 2002). Also as part of our systematic error estimate in §5, we vary this ratio. We generate a total of about 100,000 SN Ia and SN II light curves. We note that statistical error and systematic error of 2% in the flux is included in the light curve simulation.

4.1.2. Control time calculation

We calculate how many days the artificial SNe Ia can be observed. We add observation errors to the artificial SN Ia light curves. The observing errors are calculated from the limiting magnitudes of the SXDS observations, which includes the effect of decreasing signal-to-noise ratio due to the subtraction of two images.

We also include the detection efficiency in the control time calculation. The detection efficiency of the SXDS variable ob-

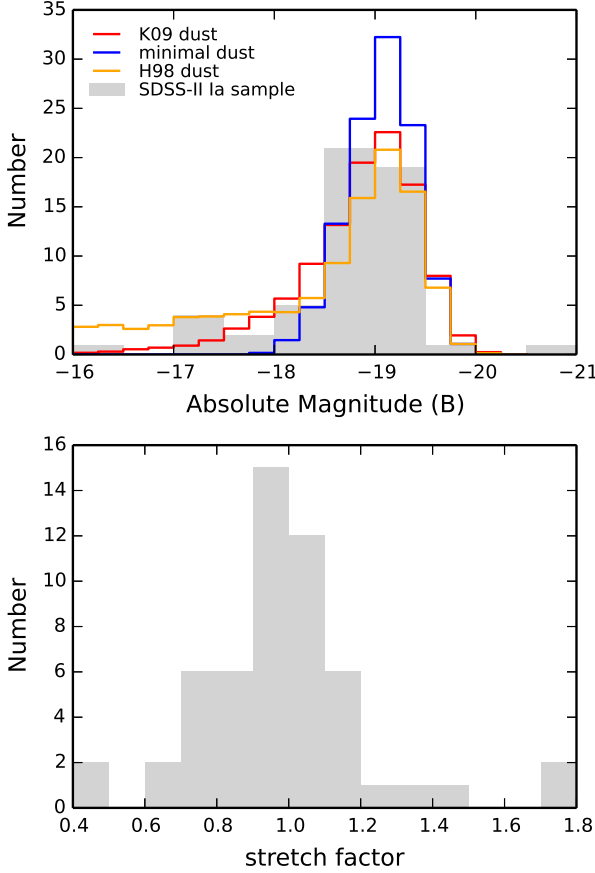


Fig. 8. The absolute magnitude (*top*) and stretch (*bottom*) distributions of the 56 $z < 0.12$ SDSS-II SNe Ia. We make artificial light curves from a SN Ia template using these distributions. Solid lines plotted in the top panel represent the simulated SN Ia distribution using assumptions in B12. The red line indicates the distribution using the dust model from Kessler et al. (2009), the blue line indicates the minimal dust model from Barbary et al. (2012), and the orange line is the dust model of Hatano et al. (1998).

ject survey was obtained by M08. M08 estimated the detection efficiency as a function of magnitude in each subtraction image. They added artificial stars to images and detected them in the same manner as for the real images. The results are shown in Figure 8 of M08.

The observable time duration (control time) of artificial SNe Ia is calculated for each redshift bin of width $\Delta z = 0.05$. The control time of SNe II is calculated in the same way as the SN Ia control time, but is only used for the estimation of contamination. Since the observations consist of 5 fields of Suprime-Cam with different survey parameters, we calculate the control times for each field, and then weight them according to field areas (see equation 3 in B12). In addition, we use the data from the center field when it overlaps with other fields. The result of the weighted control time is shown in Figure 10.

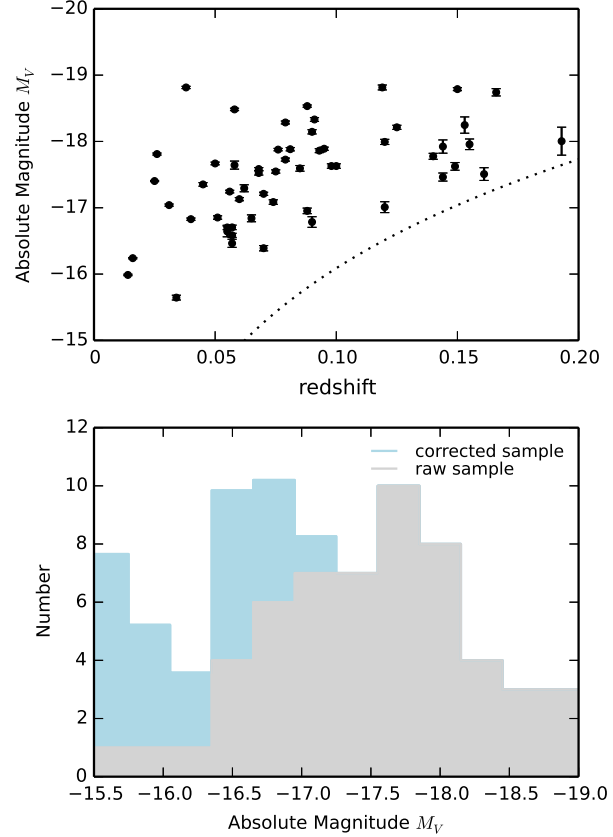


Fig. 9. The absolute magnitude and redshifts of Type II supernovae found by SDSS-II SN survey at $z < 0.17$ (*top*). The dashed line shows the 5σ detection limit of SDSS-II SN survey. At higher redshifts fainter SNe are lost, therefore we construct a luminosity function that accounts for incompleteness (*bottom*; see Equation 7). We vary the magnitude limit curve 0.2 mag brighter/fainter to estimate systematics.

4.2. Typing completeness and contamination

4.2.1. Estimating typing completeness

In order to determine the completeness of our light curve classification technique, we fit light-curve templates to our sample of artificial SNe Ia. Because the total number of observing epochs is different for the different fields of the SXDF, we calculate the completeness separately for each field. The completeness for each field (represented as 7 epoch, 6 epoch, and 5 epoch mode) is shown in the different panels of Figure 11.

As a general trend, the completeness improves as more epochs are observed (the second column of Table 1) because the maximum is easily detectable. The result also shows that SNe Ia are safely classified with high completeness (80% in average). Though this fraction is higher than the most efficient classification method in Kessler et al. 2010 ($\sim 75\%$ of Sako et al. 2011), our fitting code is only used for eliminating SNe IIL and SNe IIP from SNe Ia, whereas Kessler et al. 2010 attempted to eliminate SNe Ib/c in this way. As mentioned in §3.1.2, SNe II are more easily distinguished from SNe Ia based on light curves. Also our calculations do not include the rare luminous SNe Ib/c such as SN2005ap (Quimby et al. 2007); these will be handled as a systematic uncertainty in §5. Figure 11 also shows that when there are fewer epochs the clas-

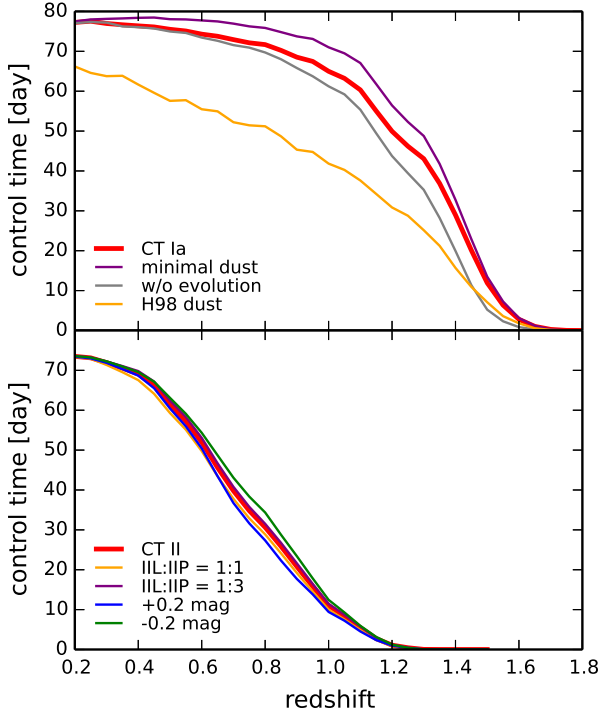


Fig. 10. *top:* The observer-frame control time for SNe Ia (red line). The models for minimal dust (purple), without evolution effects in Howell et al. 2007 (gray), and the model based on Hatano et al. 1998 (orange) are plotted as well. *bottom:* The observer-frame control time for SNe II (red line). The models for different SN IIL and SN IIP ratio (1:1 in yellow, 1:3 in purple) are plotted. In addition, the choice of magnitude limit curve in Figure 9 affects the luminosity function of SN II (see the discussion in §4.1.1). We therefore show the control time for the case of 0.2 mag brighter limit (blue) and 0.2 mag fainter limit (green).

sification becomes less secure because the epoch of maximum brightness may be missed.

4.2.2. Estimating the misclassification ratio

We also estimate how often SNe II are misclassified as SNe Ia (the contamination F_{II}). Using the same method as for SNe Ia, we made artificial SNe II and fit those SNe with light curve templates to estimate the misclassification ratio (the ratio of SN II classified SN Ia). The results are shown in Figure 12. The misclassification becomes large toward high redshift, but it is not a serious problem because the detection efficiency of SNe II is much less than that of SNe Ia at high redshift (see Figure 10).

Now, in order to find the true number (N_{Ia} in Equation 5) of SNe Ia and II at each redshift, we need to estimate the contamination of our SNe Ia sample by SNe II. There are many studies that derive core collapse supernova rates, and these results are consistent each other (Dahlen et al. 2012; Melinder et al. 2012; Graur et al. 2011; Bazin et al. 2009; Botticella et al. 2008; Mattila et al. 2012; Li et al. 2011; Smart et al. 2009; Cappellaro et al. 1999; Horiuchi et al. 2011; Magnelli et al. 2009). Since higher redshift SN II rates have larger uncertainty, we use the measured nearby SN II rate and assume that the SN II rate is increasing in proportion to the cosmic star for-

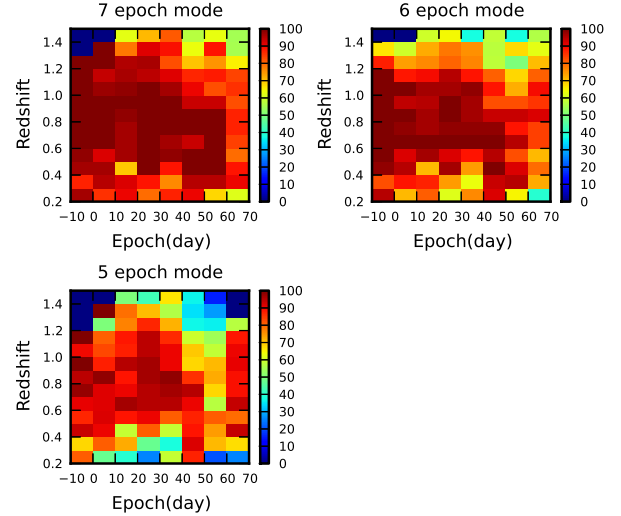


Fig. 11. The completeness of the light-curve fitting classification. These figures describe how many artificial SNe Ia are identified as Type Ia. The reliability depends on the number of observing epochs. The left top figure is for the 7 epoch observing mode (SXDF-C and SXDF-W). The right top figure is for the 6 epoch observing mode (SXDF-E). The left bottom figure is for the 5 epoch observing mode (SXDF-N and SXDF-S). The horizontal axis represents the observer-frame date of the first epoch relative to maximum light. The figures show that we can classify SNe Ia with high completeness.

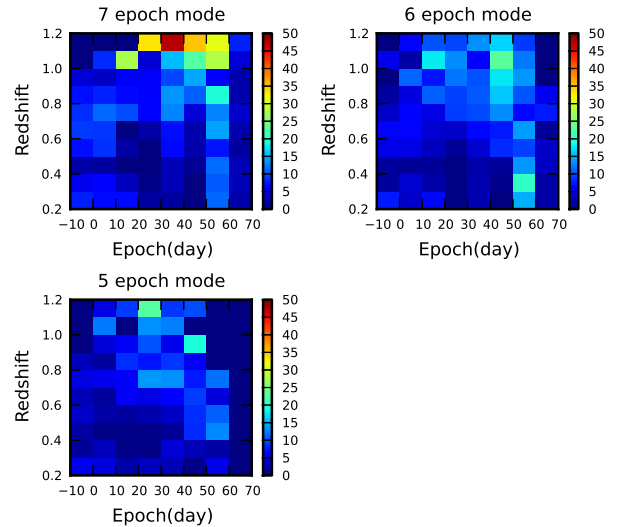


Fig. 12. The fraction, F_{II} , of instances where artificial SNe II are misclassified as SNe Ia. Three panels represent the 7 epoch, 6 epoch, and 5 epoch mode as Figure 11. The misclassification increases toward high redshift. In contrast, the detection efficiency of SNe II decreases toward high redshift. As a result, the contamination is also small at high redshift.

mation rate. The progenitors of SNe II are massive stars and have a very short delay time between star formation and explosion, which justifies this assumption. We use a nearby SN II rate of $0.394 \times 10^{-4} \text{ yr}^{-1} \text{ Mpc}^{-3}$ (Li et al. 2011) at $z \sim 0$, and a star formation rate $\propto (1+z)^{3.6}$ (Hopkins & Beauchamp 2006). The SN II rate is then $0.394 \times (1+z)^{3.6}$. Using this assumption, the number of SNe II available that potentially could be misclassified as SNe Ia, $N_{II}(z)$, can be calculated using the equation below.

$$N_{II}(z) = \int 0.394 \times (1+z)^{3.6} \frac{CT_{II}(z)}{1+z} \frac{\Theta}{4\pi} V(z) dz, \quad (8)$$

where $CT_{II}(z)$ represents the control times of SNe II. We note in particular that this model for the SN II rates is in agreement with the $z \sim 1$ SN II rate from Dahlen et al. (2012).

4.2.3. SN Ib/c contamination

In this subsection, we estimate the number of SNe Ib/c in our sample of 39 SNe Ia. In addition to the 2 SNe Ib/c that are found from their colors, we estimate that there are another $3.15^{+4.20}_{-2.10}$ SNe Ib/c are in the sample. We compare this number with the number that one would infer from evolving local SNe Ib/c rates to higher redshift and we estimate the redshift distribution of the SNe Ib/c in our SN Ia sample.

As described in §3.1.4, the candidate refinement indicates that approximately 2 out of the 14 SNe I with color information are SNe Ib/c. This yields an estimated observed SN Ib/c contamination percentage of $14.3^{+18.8}_{-9.2}$ based on the combined application of lightcurve shape and color-color selection.

Of the 39 lightcurve-selected SN Ia candidates 8 have spectroscopic confirmation and an additional 10 possess colors expected for SNe Ia, leaving a pool of 21 lightcurve-selected candidates that could still harbour SNe Ib/c. While it is encouraging that color classification has revealed only minor contamination from SNe Ib/c, the implication is that roughly 3 additional SNe Ib/c remain in this unconfirmed pool. For these a statistical correction can be applied if their number and redshift distribution can be estimated.

Since spectroscopically-confirmed SNe Ia are not present in the unconfirmed pool, it could be argued that such objects should also be removed from the color-color classified subsample. The rationale here is that since spectroscopic observations may suffer greater selection biases than color observations, the set of spectroscopically-confirmed objects may be less representative of the unconfirmed pool than is the set of objects with colors. Kolmogorov-Smirnov tests of either the redshift distributions or the peak magnitudes indicate that the spectroscopically-confirmed and color-color subsamples are consistent with the unconfirmed pool with $P = 0.74$. While there is no direct evidence of differential bias, this approach may be considered more conservative. In this case the removal of 2 spectroscopically-typed SNe from the sample of 14 objects with color-color information would raise the observed contamination rate to 2 out of 12 objects, or $16.7^{+21.9}_{-10.8}\%$.

While correlated, these various estimates are consistent with a SN Ib/c contamination rate of $15^{+20}_{-10}\%$. Though the uncertainty is large due to the small number of color samples, we adopt this rate for the unconfirmed subsample. This would imply an additional $3.15^{+4.20}_{-2.10}$ undetected SNe Ib/c in the uncon-

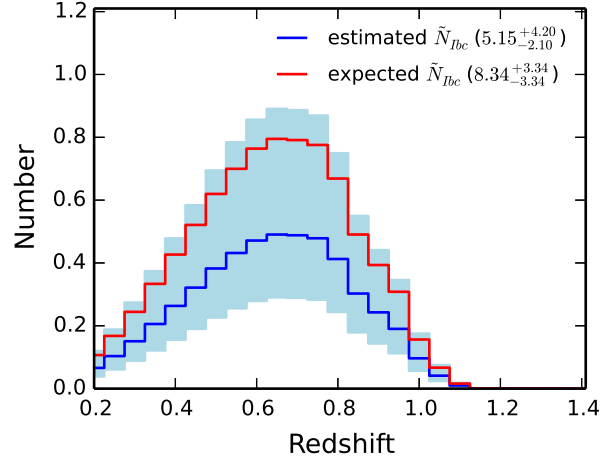


Fig. 13. The estimated number of possible SNe Ib/c contamination ($N_{Ib/c}$ in Equation 5) in the lightcurve-selected SN I sample. The red solid line indicates the expected number simulated assuming nearby SN Ib/c rate and its evolution (Li et al. 2011, Dahlen et al. 2012). The blue solid line and light blue region represents the number estimated from color-color selection and corresponding error region.

firmed pool. Combined with the 2 SNe Ib/c detected via color selection this leads to a estimated total of $5.15^{+4.20}_{-2.10}$ SNe Ib/c in the lightcurve-shape selected sample. This residual SN Ib/c contamination is treated as a systematic uncertainty.

The second component of the statistical correction of the unconfirmed pool is to determine the expected redshift distribution. The core collapse SN rate, the SN Ib/c luminosity function and the survey control time must then be included to predict the final redshift distribution. Figure 13 shows the result of such a calculation using the luminosity function of SN Ib/c from nearby complete survey (Li et al. 2011) to calculate the control time, and assuming the observed fraction of SN Ib/c to SN Ia (Li et al. 2011) and core-collapse SN rate evolution (Dahlen et al. 2012). The expected number of contaminating SNe Ib/c is $8.34^{+3.34}_{-3.34}$. This number is consistent with the number estimated directly from the observation, $5.15^{+4.20}_{-2.10}$. The two objects, 2-038 and 4-100, classified as a SN Ib/c via their color are at $z \sim 0.45$ and $z \sim 0.75$, respectively — right near the peak of the calculated distribution in Figure 13.

In summary, we estimate that a total of $5.15^{+4.20}_{-2.10}$ SNe Ib/c contaminate the lightcurve-selected SN I sample. We use color information to directly remove objects 2-038 and 4-100. The remaining $3.15^{+4.20}_{-2.10}$ SNe are subtracted using the redshift distribution of Figure 13 using the appropriate scaling. Since we have only a limited color sample to estimate SN Ib/c contamination, the impact of the uncertainty is large in the lowest bin ($0.2 < z < 0.6$), and is comparable to the Poisson uncertainties associated with the detected SN Ia sample (Table 4). However, this effect becomes much smaller beyond $z = 0.6$, where we want to constrain the rate. We note that reasonable changes to the color selection procedure, or to the shape of the SN Ib/c redshift distribution, have negligible effect relative to the Poisson errors.

5. Results and systematic error estimation

The SN Ia rate is obtained from Equations 3–5. The observed number (N_{Ia}) of SNe Ia in each redshift bin is obtained from Equation 5, and is shown in Figure 14. We show the SN Ia rate in each redshift bin of $\Delta z = 0.4$ in Table 5. The results include systematic and statistical errors. These redshift bins are the same as those of Dahlen et al. (2008). The effective redshift \bar{z} of each bin is the average redshift in the bin, weighted by the control time and volume, and is given by

$$\bar{z} = \frac{\int_{z_1}^{z_2} z \frac{CT_{Ia}(z)}{1+z} V(z) dz}{\int_{z_1}^{z_2} \frac{CT_{Ia}(z)}{1+z} V(z) dz}. \quad (9)$$

We now itemize the causes of systematic uncertainties and the methods used to estimate their sizes, and then summarize the results in Table 4.

(1) In generating artificial SNe II, we adopted a ratio of Type II-P to Type II-L of 2:1 (Richardson et al. 2002). However the real distribution of Type II subtypes is not well-known. Using a different ratio will change the fraction of misclassifications of SN II as SN Ia, F_{II} . We adopt different ratios of 1:1 and 3:1 and recalculate the SN Ia rates in each case. As plotted in Figure 10, the effect of changing the ratio is minor (up to $\sim 2\%$). The impact on the final SN Ia rate depends on the redshift range (shown in Table 4).

(2) Artificial SNe II were generated using the peak magnitude distribution of low-redshift SNe II found by the SDSS-II SN survey. Since the observed luminosity distribution is not complete for fainter SNe II, we carefully corrected the magnitude distribution using the magnitude limit curve (see the discussion in §4.1.1). We checked how the correction factor changes if the magnitude limit is moved 0.2 mag brighter/fainter. As in Figure 10, the effect of changing this threshold is minor; resulting in $\sim 2\%$ changes in the rate. We take the half of this difference as a systematic.

(3) In our baseline calculation we accounted for contamination from SNe Ib/c by color-color selection discussed in §3.1.4. This makes $3.15^{+4.20}_{-2.10}$ additional SN Ib/c contaminating the SN Ia sample after removing two objects classified as SN Ib/c (2-038 and 4-100). The effect of changing the number of SN Ib/c is greatest in the lowest-bin. In a bin with small number of SN Ia, the contamination from SN Ib/c can be the biggest uncertainty. This means that more color information would have helped to better constrain the rate at $z < 0.6$, and such color information will be important in future surveys.

(4) In §3.1.3, we removed two likely AGN. There remained one source near core without X-ray detections or spectroscopic or color constraints. If that source were an AGN, or if one of the rejected X-ray detections were a SN Ia, the resulting error would be 2.6%. We take this as the systematic error due to AGN (i.e., $\tilde{N}_{AGN} = 1$ in equation 5).

(5) We separately consider the contamination from the core collapse SNe in the high-redshift bin ($1.0 \leq z < 1.4$). As noted in §3.3, the control time for Type II SNe is very small at $z \geq 1.0$, but there might exist very bright core collapse SNe. Boissier & Prantzos (2009) show the magnitude distribution of SNe Ib/c and II from a large but heterogenous sample. Most of these SNe are fainter than ~ -18.0 mag and there are very few bright

SNe of ~ -19.0 mag. However the magnitudes are discovery magnitudes, and serve only as lower limits on the peak magnitudes. The Ib/c sample of Richardson et al. (2006) contains three very bright SNe Ic that would be detectable and possibly mistaken for SNe Ia at high-redshift ($z > 1.0$). We estimate the contamination ratio of bright SNe using the magnitude distribution of Figure 6 of Bazin et al. (2009). There are four core collapse SNe (one object is a SN Ib/c and three objects are SNe II) that have peak absolute magnitudes that are around -19 . In this figure, there are approximately 50 SNe Ia with a similar magnitude. Therefore the contamination from core collapse SNe in the high-redshift bin is estimated to be $\sim 8\%$.

(6) In the control time calculation we assumed that the average stretch changes with redshift in the manner prescribed by to Howell et al. (2007). If instead we recalculate the control time using the local stretch distribution in every redshift bin we find a somewhat lower control time in the highest redshift bin, leading to a $\sim 15\%$ increase in the estimated SN Ia rate for $1.0 \leq z < 1.4$. This is the dominant source of systematic uncertainty in this bin.

(7) The effect from the dust extinction of host galaxy is the most uncertain factor in the rate calculation. Recall that the sample used for the control calculation was based on SNe Ia uncorrected for dust extinction. This sample has a tail extending fainter than the $M_B \sim -18.0$ limit given by the minimal dust model. Thus, if the minimal dust model is taken as a reference, our rates decrease by 2.9%, 6.5%, and 11.9%, respectively, in each redshift bin. If instead extinction is much stronger than in our observed reference sample, our rates will be underestimated. B12 examined various dust models to investigate the extinction effects. According to their estimate, the most extreme dust model based on Hatano et al. 1998 (“dust model A” in their paper) resulted in up to 50% changes in rates. Though our approach is different from B12 (i.e., they constructed SN Ia luminosity function from two parameter families), we examined how large the effect of this extreme dust model is. We simulated the control time in the same manner as B12 (see Figure 10), and estimated the differences to be +28.2%, +43.0%, and +47.8%, respectively, in each redshift bin. This result is consistent with the estimate of B12. We wish to include this as a systematic uncertainty, but we will report it separately in the systematics in Table 4 because, unlike other systematics, the size of this systematic is highly speculative.

Several studies have indicated that the mean extinction increases with redshift (Mannucci et al. 2007; Holwerda 2008), so this issue may be most important in our highest redshift bin. B12 took a systematic uncertainty of 50% due to possible unaccounted for dust extinction. As examples, in Figure 15 we show uncertainties of 50%, and that of the minimal dust model. We note that even though the extinction-corrected rate is uncertain, our base measurement is a good representation of the rate to be used for predicting future SN searches at high redshift.

6. Discussion

6.1. SN Ia rate function

We fit the SN Ia rates with a power law (e.g., Pain et al. 2002),

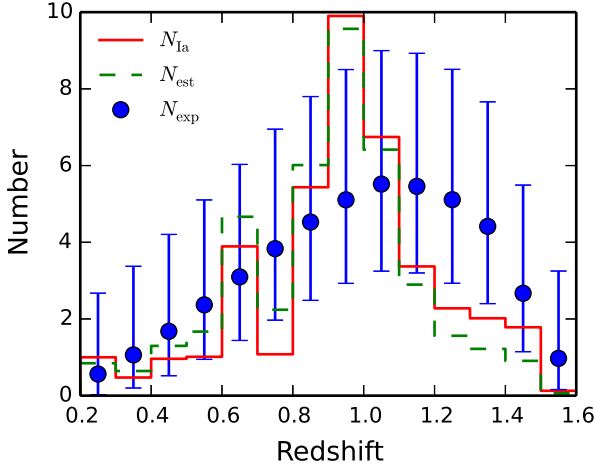


Fig. 14. The number of SNe Ia from SXDS observations. The green dashed histogram indicates the estimated number (N_{est}) of SN Ia candidates obtained by the light-curve fitting. The red solid histogram indicates the observed number (N_{Ia}) of SNe Ia, after correction for completeness and contamination. The blue points with statistical error bars indicate the expected number (N_{exp}) obtained by the model-dependent rate calculation of Equation 3. In this figure, one SN Ia, 1-081, at $z = 1.45$ is included in the histogram.

$$r_V(z) = r_0(1+z)^\alpha. \quad (10)$$

In this fit, we use the SN Ia rate obtained in redshift bins of $\Delta z = 0.1$. The best fit values of r_0 and α are

$$r_0 = 0.20^{+0.52}_{-0.16}(\text{stat.})^{+0.26}_{-0.07}(\text{syst.}) \times 10^{-4} \text{yr}^{-1} \text{Mpc}^{-3} \quad (11)$$

$$\alpha = 2.04^{+1.84}_{-1.96}(\text{stat.})^{+2.11}_{-0.86}(\text{syst.}) \quad (12)$$

We show the fit in Figure 15, and the expected number (N_{exp}) obtained by this fit in Figure 14.

6.2. Comparison with previous SN rate studies

Here, we check the consistency of our results with previous works (Figure 16). First, we compare nearby and mid-redshift SN Ia rates with our results. Li et al. (2011) derived a nearby SN Ia rate from 274 SNe Ia from the Lick Observatory Supernova Search (LOSS). Dilday et al. (2008) measured the nearby SN Ia rate at $z = 0.12$ using SNe Ia obtained by the SDSS-II SN survey. Recently, Perrett et al. (2012) determined the SN Ia rate in $0.1 \leq z \leq 1.1$ range with a very small uncertainty using the dataset of SNLS. These results are quite consistent with our fitted power-law curve. We also compare our measurements to those at similar or slightly higher redshifts. Graur et al. (2011; hereafter Gr11) obtained high-redshift SN Ia rates in the Subaru Deep Field (SDF) using the multi-color SED fitting classification method (Poznanski et al. 2007a). Gr11 carried out very deep photometric observations and detected very high-redshift SNe Ia up to $z \sim 2.0$. They used one epoch with a reference epoch, and thus could not employ our light curve fitting method.

On the other hand, Dahlen et al. (2008; hereafter Da08) identified SNe with spectroscopic observations of GOODS SN survey, and measured SN Ia rates up to $z \sim 1.6$. B12 also derived SN Ia in this same redshift range from *Hubble Space Telescope* Cluster Supernova Survey. Even though these stud-

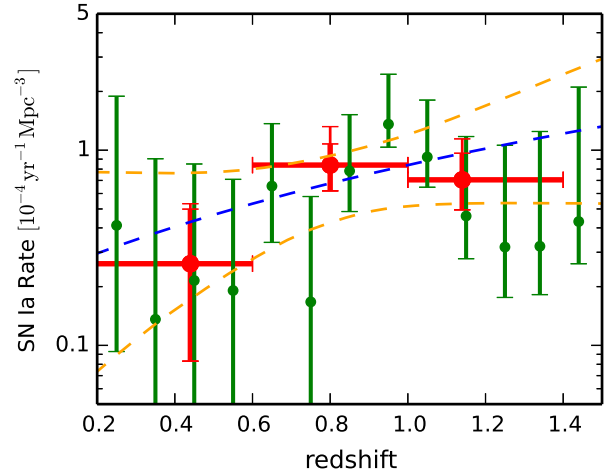


Fig. 15. SN Ia rates in SXDF. Red circles show the rate in redshift bins of width $\Delta z = 0.4$, the same bin width used by Dahlen et al. (2008), calculated using Equation 4. Green crosses show the rate in redshift bins of width $\Delta z = 0.1$. For the upper error bar in $\Delta z = 0.4$ rates, the 2nd bar represents the observed + known systematics and the top bar represents the case of adding 50% *ad hoc* errors for the dust extinction. The blue dashed line shows $r_V(z) = r_0(1+z)^\alpha$, where $r_0 = 0.20^{+0.52}_{-0.16}(\text{stat.})^{+0.26}_{-0.07}(\text{syst.}) \times 10^{-4} \text{yr}^{-1} \text{Mpc}^{-3}$, and $\alpha = 2.04^{+1.84}_{-1.96}(\text{stat.})^{+2.11}_{-0.86}(\text{syst.})$. The orange dashed lines correspond to the $\pm 1\sigma$ error region.

ies used different samples and techniques, our result and the results from these studies are consistent within the uncertainties.

In the highest redshift regime ($z \gtrsim 1.4$), the SN Ia rate is still uncertain. Gr11 show that the SN Ia rate remains high beyond this redshift, while the SN Ia rates of Da08 are flat from $z \sim 0.8$ to $z \sim 1.2$, and then show a sharp decline at $z \sim 1.6$. As noted in §5, B12 also found that different assumptions about host-galaxy dust extinction can induce systematic differences between measurements. It is therefore not yet clear if we have observed the peak in the volumetric SN Ia rate. According to galaxy studies (e.g., Hopkins & Beacom 2006), the peak of the cosmic star formation rate is at $z \sim 2-3$. Based on the peak in the cosmic star formation rate, we estimate that the delay time of SNe Ia at high redshifts is $\lesssim 2-3$ Gyr. In order to determine whether SNe Ia with the shortest delay times are dominant or not, it is necessary to observe more samples at $z \geq 1.4$. This will be a key issue for future SN Ia surveys. One of these is the HSC transient survey, which will use *Hyper Suprime-Cam* on the Subaru Telescope. In this survey, ~ 100 SNe Ia will be detected with $z \gtrsim 1.0$, and thus provide useful information about the high-redshift SN Ia rates. At the same time, at low redshift it will construct a complete sample of SNe of all types, to faint luminosities and/or high values of dust extinction. Both the luminosity and extinction distributions will help in refining future rates calculations at high redshift.

We also check for consistency with Totani et al. (2008; hereafter To08). To08 measured the delay time distribution of SNe Ia using the same variable object catalog of M08, but used a different method to select SNe Ia. To08 selected 65 SN Ia candidates showing significant spatial offset from the center of host galaxies with an old stellar population. However, not

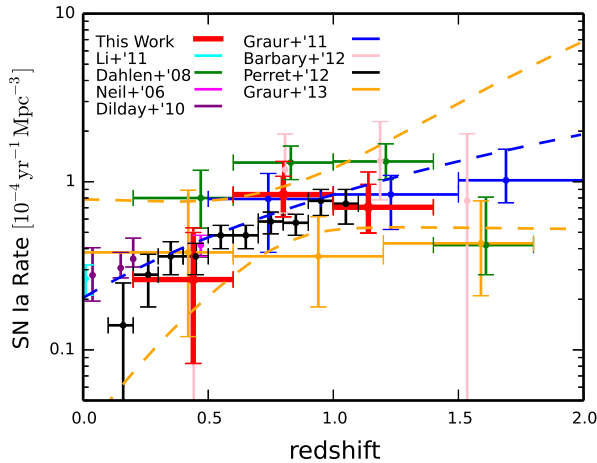


Fig. 16. Comparison of various previous works with our results. The *red data* show our results. As in Figure 15, the systematic uncertainty is divided into observed + known systematics (2nd error bar), and the case of adding 50% *ad hoc* errors for the dust extinction (top error bar). The *cyan data* are the results by Li et al. (2011). The *green data* are the results by Dahlen et al. (2008). The *pink data* is the result at $z = 0.47$ by Neill et al. (2006). The *purple data* is the result by Dilday et al. (2010). The *blue data* are the result of Graur et al. (2011). The *light pink data* are the result of Barbary et al. (2012). The *black data* are the result of Perrett et al. (2012). The *orange data* are the result of Graur et al. (2013).

all of their candidates are SNe Ia due to the uncertainty in the selection method. To08 estimated that 82% of the 65 candidates were actually SNe Ia. We check their candidates by our light-curve fitting method. Out of the 65 candidates in To08, 19 candidates have light curves with a sufficient number of epochs and sufficient signal-to-noise to perform our light-curve fitting. Fifteen candidates (79% of the 19 candidates) are identified as SNe Ia. This result indicates that our selection of SNe Ia is consistent with the selection of To08.

7. Conclusions

In this paper we have presented new measurements of the high-redshift SN Ia rate, using objects selected from the SXDS variable object survey. Each variable object was observed in the i' -band at 5-7 epochs for about two months, which is sufficient to build light curves. The variable objects are classified by comparing their light curves with template light curves. Out of 1040 variable objects, 44 SN I candidates are selected. After excluding a SN Ia beyond $z = 1.4$, and using ancillary data to exclude two likely AGNs and two likely SNe Ib/c, we construct a sample of 39 SNe Ia that are then used to derive the rates. Using simulated light curves, we correct the number of SN Ia candidates for incompleteness due to misclassification. The control time is also calculated with artificial SN light curves. Finally, we derive the SN Ia rate in several redshift bins between $0.2 < z < 1.4$. Our rate measurements are the most distant yet obtained using light curves from ground-based telescopes. We have considered a number of systematic factors affecting the rates. Chief among these is the correction for extinction. However, even using conservative estimates of the systematic error, the statistical errors are comparable in size.

Improved systematics control will be much more important for future rates measurements based on much larger samples.

Our SNe Ia rates are consistent with the rates that have been derived in earlier studies. Up to $z \sim 1.4$, the rate continues to increase and is well described by a simple power law. The SDXS survey was relatively inefficient at finding SNe Ia beyond $z \sim 1.4$, so we are unable to either confirm or refute the downturn that has been seen in searches done with HST beyond this redshift. The upcoming HSC transient survey is considerably more efficient in finding SNe beyond $z \sim 1.4$ than the SXDS survey, thus offering us the possibility of measuring the rates of SNe Ia in this important redshift range with unprecedented precision.

We would like to thank the Subaru Telescope staff for their invaluable assistance. This work was supported in part with scientific research grants from the Ministry of Education, Science, Culture, and Sports, Science and Technology (MEXT) of Japan, and by the grant-in-aid for the Global COE Program "The Next Generation of Physics, Spun from Universality and Emergence" from MEXT. J.O., Y.I. and T.M. has been financially supported by the Japan Society for the Promotion of Science (JSPS) through the JSPS Research Fellowship. This work was also supported in part by the Director, Office of Science, Office of High Energy and Nuclear Physics and the Office of Advanced Scientific Computing Research, of the U.S. Department of Energy (DOE) under Contract Nos. DE-FG02-92ER40704, DE-AC02-05CH11231, DE-FG02-06ER06-04, and DE-AC02-05CH11231.

References

- Akiyama, M., et al. in preparation
- Alard, C., & Lupton, R. H. 1998, *ApJ*, 503, 325
- Alard, C. 2000, *A&AS*, 144, 363
- Amanullah, R., Lidman, C., Rubin, D., et al. 2010, *ApJ*, 716, 712
- Arnouts, S., Cristiani, S., Moscardini, L., et al. 1999, *MNRAS*, 310, 540
- Astier, P., et al. 2006, *A&A*, 447, 31
- Barris, B. J., & Tonry, J. L. 2006, *ApJ*, 637, 427
- Barbary, K.; Aldering, G.; Amanullah, R. 2012, *ApJ*, 745, 31
- Bazin, G., et al. 2009, *A&A*, 499, 653
- Bloom, J. S., Kasen, D., Shen, K. J., et al. 2012, *ApJ*, 744, L17
- Blondin S., Prieto J. L., Patat F., Challis P., 2009, *ApJ*, 693, 207
- Boissier S. & Prantzos N., 2009, *A&A*, 503, 137
- Bolzoni, M., Miralles, J.-M., & Pell. R. 2000, *A&A*, 363, 476
- Botticella, M.T., et al. 2008, *A&A*, 479, 49
- Brown, P. J., et al. 2012, *ApJ*, 753, 22
- Bruzual, G., & Charlot, S. 2003, *MNRAS*, 344, 1000
- Buta, R. J. 1982, *PASP*, 94, 578B
- Cappellaro, E., Evans, R., & Turatto, M. 1999, *A&A*, 351, 459
- Chomiuk, L., Soderberg, A.M., Moe, M., et al., 2012, *ApJ*, 750, 164
- D'Andrea, C., et al. 2010, *ApJ*, 708, 661
- Dahlen, T., et al. 2008, *ApJ*, 681, 462
- Dahlen, T., et al. 2012, *ApJ*, 757, 70D
- De Vaucouleurs, G. et al. 1981, *PASP*, 93, 36D
- Dilday, B. et al. 2008, *ApJ*, 682, 262D
- Fassia, A. et al. 2000, *MNRAS*, 318, 1093F
- Fioc, M. & Rocca-Volmerange, B., 1997, *A&A* 326, 950
- Fioc, M. & Rocca-Volmerange, B., 1999, *A&A*, 351, 869
- Frieman, J. A., et al. 2008, *AJ*, 135, 338F

- Furusawa, H., et al. 2008, *ApJS*, 176, 1F
- Geier, S. et al., 2007, *A&A*, 464, 299
- González Hernández, J. I., et al. 2009, *ApJ*, 691, 1
- Graur, O., et al. 2011, *MNRAS*, 417, 616
- Graur, O., et al. 2013, *arXiv:1310.3495*
- Hachisu, I., Kato, M., & Nomoto, K. 1996, *ApJ*, 470, L97
- Hachisu, I., Kato, M., & Nomoto, K. 2008, *ApJ*, 683, L127
- Hancock, P., Gaensler, B.M., Murphy, T., 2011, *ApJ* 735, L35.
- Hatano, K., Branch, D., & Deaton, J. 1998, *ApJ*, 502, 177
- Hicken, M., et al. 2009, *ApJ*, 700, 1097
- Holwerda, B. W. 2008, *MNRAS*, 386, 475
- Hopkins, A. M., & Beacom, J. F., 2006, *ApJ*, 651, 142
- Horiuchi, S., Beacom, J. F., Kochanek, et al. 2011, *ApJ*, 738, 154
- Howell, D. A., Sullivan, M., Conley, A., and Carlberg, R., 2007, *ApJ*, 667, L37
- Hsiao, E. Y., Conley, A., Howell, D. A., et al. 2007, *ApJ*, 663, 1187
- Iben, I. Jr., & Totukov, A. V. 1984, *ApJS*, 54, 335
- Ihara, Y., et al. 2007, *PASJ*, 59, 811
- Ilbert, O., et al. 2006, *A&A*, 457, 841
- Kerzendorf, W. E., et al. 2009, *ApJ*, 701, 1665
- Kessler, R., Becker, A. C., Cinabro, D., et al. 2009, *ApJS*, 185, 32
- Kessler, R., Bassett, B., Belov, P, et al. 2010, *PASP*, 122, 1415
- Knop, R. A., et al. 2003, *ApJ*, 598, 102
- Koester, D., et al. 2005, *A&A*, 432, 1025
- Kowalski, M., et al., 2008, *ApJ*, 686, 749
- Kuznetsova, N., et al. 2008, *ApJ*, 673, 981
- Ruiz-Lapuente, P., et al. 2004, *Nature*, 431, 1069
- Leonard, D. C., et al. 2002, *PASP*, 114, 35
- Leonard, D. C., et al. 2002, *AJ*, 124, 2490
- Li, W., et al. 2011, *MNRAS*, 412, 1441
- Lidman, C., et al. 2005, *A&A*, 430, 843
- Lonsdale, S. et al. 2004, *ApJS*, 154, 54
- Madau, P., Della Valle, M., & Panagia, N. 1998, *MNRAS*, 297, L17
- Mannucci, F., et al. 2005, *A&A*, 433, 807
- Mannucci, F., Della Valle, M., & Panagia, N. 2006, *MNRAS*, 370, 773
- Mannucci, F., Della Valle, M., & Panagia, N. 2007, *MNRAS*, 377, 1229
- Magnelli, B., Elbaz, D., Chary, R. R., et al. 2009, *A&A*, 496, 57
- Maguire, K., Sullivan, M., Patat, F., et al. 2013, *MNRAS*, 436, 222
- Mattila, S., Dahlen, T., Efsthathiou, A., et al. 2012, *ApJ*, 756, 111
- Maoz, D., & Mannucci, F., 2008, *MNRAS*, 388, 421
- Maoz, D., & Mannucci, F. 2012, *PASA*, 29, 447
- Margutti, R., Soderberg, A. M., Chomiuk, L., et al. 2012, *ApJ*, 751, 134
- Melinder, J., Dahlen, T., Mencía Trinchant, L., et al. 2012, *A&A*, 545, 96
- Miyazaki, S., et al. 2002, *PASJ*, 54, 833
- Morokuma, T., et al. 2008, *ApJ*, 676, 163
- Morokuma, T., et al. 2008, *ApJ*, 676, 121
- Morokuma, T., et al. 2010, *PASJ*, 62, 19
- Neill, J.D., et al. 2006, *AJ*, 132, 1126
- Nomoto, K. 1982, *ApJ*, 253, 798
- Nomoto, K., Iwamoto, K., & Kisimoto, N. 1997, *Sci*, 276, 1378
- Nugent, P., Kim, A., & Perlmutter, S. 2002, *PASP*, 114, 803
- Nugent, P. E., Sullivan, M., Cenko, S. B., et al. 2011, *Nature*, 480, 344
- Oda, T. et al. 2008, *PASJ*, 60, 169
- Pain, R. et al. 2002, *ApJ*, 577, 120
- Panagia, N., Van Dyk, S.D., Weiler, K.W., et al., 2006, *ApJ*, 646, 369.
- Patat, F. et al. 2007, *A&A*, 474, 931
- Pérez-Montero, E., et al. 2007, *MNRAS*, 381, 125
- Perlmutter, S. et al., 1997, *ApJ*, 483, 565
- Perlmutter, S. et al., 1999, *ApJ*, 517, 565
- Perrett, K., Sullivan, M., Conley, A., et al., 2012, *ApJ*, 144, 59
- Poznanski, D., Maoz, D., and Gal-Yam, A. 2007, *AJ*, 134, 1285P
- Poznanski, D., et al. 2007, *MNRAS*, 382, 1169P
- Pritchett, C., Howell, A, and Sullivan, M. 2008, *ApJL*, 683, 25
- Quimby, R., et al. 2007, *ApJ*, 668, L99
- Raskin C., Kasen D., 2013, *ApJ*, 772, 1
- Richardson et al. 2002, *AJ*, 123, 745
- Richardson, D., Branch, D., & Baron, E. 2006, *AJ*, 131, 2233
- Riess, A. G., et al. 1998, *AJ*, 116, 1009,
- Riess, A. G., et al. 2007, *ApJ*, 659, 98
- Rola, C. et al. 1997, *MNRAS*, 289, 419
- Sako, M. et al. 2008, *AJ*, 135, 348S
- Sako, M. et al. 2011, *ApJ*, 738, 162S
- Sako, M. et al., in preparation
- Scalo, J. M. 1986, *Fundam. Cosmic Phys.*, 11, 1
- Schaefer, B. E. & Pagnotta, A. 2012, *Nature*, 481, 164
- Sekiguchi, K. et al., 2004, *BAAS*, 205, 8105
- Shen K. J., Guillochon J., Foley R. J., 2013, *ApJ*, 770, L35
- Joshua D. Simon. et al., 2009, *ApJ*, 702, 1157
- Smartt, S. J., Eldridge, J. J., Crockett, R. M., & Maund, J. R. 2009, *MNRAS*, 395, 1409
- Sternberg A. et al., 2011, *Sci*, 333, 856
- Stritzinger M. et al., 2010, *AJ*, 140, 2036
- Sullivan, M. et al., 2006, *ApJ*, 648, 868
- Sullivan, M., et al. 2011, *ApJ*, 737, 102
- Suzuki, N., et al., 2012, *A&A*, 746, 85
- Takanashi, N., Doi, M., & Yasuda, N. 2008, *MNRAS*, 389, 1577
- Tonry, J. L., Schmidt, B. P., Barris, B., et al. 2003, *ApJ*, 594, 1
- Totani, T, et al., 2008, *PASJ*, 60, 1327
- Ueda, Y, et al., 2008, *ApJS*, 179, 124
- Wang, L., et al. 2006, *ApJ*, 641, 50
- Wang, B., & Han, Z. 2012, *NewAR*, 56, 122W
- Warren, S. et al. 2007, *MNRAS*, 375, 213
- Webbink, R. 1984, *ApJ*, 277, 355
- Wood-Vasey, W. M., et al. 2007, *ApJ*, 666, 694
- Yasuda, N., & Fukugita, M. 2010, *AJ*, 139, 39

Table 1. Summary of Suprime-Cam photometry.

Field	Epoch ^a	Date (UT) ^b	Δt ^c	t_{exp} [sec]	Seeing ["] ^d	m_{lim} ^e
<i>i'</i> -band						
SXDF-C	1	02/09/29,30	0.0	2700	0.54	26.19
SXDF-C	2	02/11/01	32.6	1860	0.92	25.76
SXDF-C	3	02/11/02	33.5	1800	0.68	25.85
SXDF-C	4	02/11/05	36.7	2400	0.70	26.11
SXDF-C	5	02/11/09	40.5	2460	0.60	25.77
SXDF-C	6	02/11/27,29	59.8	4200	0.72	26.38
SXDF-C	7	02/12/07	68.4	3000	0.78	26.32
SXDF-C	8	03/10/20	385.7	5760	1.14	26.53
SXDF-C	9	03/10/21	386.5	7500	0.58	26.71
SXDF-C	10	05/09/28	1094.6	3600	1.00	26.04
SXDF-N	1	02/09/29,30	0.0	3300	0.56	26.26
SXDF-N	2	02/11/01	32.4	2640	0.96	25.88
SXDF-N	3	02/11/02	33.3	1800	0.68	25.86
SXDF-N	4	02/11/09	40.3	2100	0.64	25.78
SXDF-N	5	02/11/29	60.3	3300	0.74	26.27
SXDF-N	6	03/09/22	357.5	4264	0.60	26.37
SXDF-N	7	03/10/02	367.6	1500	0.70	25.88
SXDF-N	8	03/10/21	386.5	3000	0.72	26.14
SXDF-S	1	02/09/29,30	0.0	3300	0.52	26.28
SXDF-S	2	02/11/01	32.5	3600	1.04	25.91
SXDF-S	3	02/11/02	33.4	1800	0.70	25.83
SXDF-S	4	02/11/09	40.4	2580	0.66	25.60
SXDF-S	5	02/11/29	60.6	1500	0.82	26.00
SXDF-S	6	03/09/22	357.6	4500	0.54	26.45
SXDF-S	7	03/10/02	367.7	2040	0.68	26.00
SXDF-S	8	05/09/28	1094.6	3900	0.96	26.04
SXDF-E	1	02/09/29,30	0.0	3300	0.60	26.25
SXDF-E	2	02/11/01	32.5	3000	1.04	25.97
SXDF-E	3	02/11/02	33.4	1800	0.70	25.83
SXDF-E	4	02/11/09	40.4	2820	0.66	26.78
SXDF-E	5	02/11/29	60.6	1800	0.80	26.03
SXDF-E	6	02/12/07	68.6	1209	1.54	25.19
SXDF-E	7	03/09/22	357.6	6000	0.62	26.58
SXDF-E	8	03/10/02	367.7	1271	0.68	25.71
SXDF-E	9	03/10/21	386.7	1400	0.88	25.51
SXDF-E	10	05/09/28	1094.6	3600	0.96	26.11
SXDF-W	1	02/09/29,30	0.0	2400	0.54	26.14
SXDF-W	2	02/11/01	32.7	3000	0.96	25.96
SXDF-W	3	02/11/02	33.5	1800	0.66	25.84
SXDF-W	4	02/11/05	36.8	3060	0.76	25.98
SXDF-W	5	02/11/09	40.5	2100	0.64	25.97
SXDF-W	6	02/11/27,29	59.8	4200	0.74	26.39
SXDF-W	7	02/12/07	68.5	6483	1.04	26.34
SXDF-W	8	03/10/20,21	386.5	5460	0.66	26.46
<i>R_c</i> -band						
SXDF-N	1	02/11/01	32.5	2400	0.85	26.37
SXDF-N	2	02/11/09	40.5	1920	0.81	26.02
SXDF-N	3	08/01/09	1927.3	2400	0.79	26.41
SXDF-S	1	02/11/01	32.6	2400	0.83	26.32
SXDF-S	2	02/11/09	40.6	1920	0.71	26.29
SXDF-S	3	08/01/09	1927.4	2400	0.69	26.52
SXDF-E	1	02/11/01	33.6	2400	0.89	26.26
SXDF-E	2	02/11/09	40.6	1920	0.87	26.12
SXDF-E	3	08/01/09	1927.4	2400	0.73	26.46

Table 1. (Continued.)

Field	Epoch ^a	Date (UT) ^b	Δt ^c	t_{exp} [sec]	Seeing ["] ^d	m_{lim} ^e
SXDF-W	1	02/11/01	33.7	3360	0.91	26.27
SXDF-W	2	02/11/09	40.7	1920	0.65	25.92
SXDF-W	3	08/01/09	1927.5	2400	0.81	26.33
<i>z'</i> -band						
SXDF-N	1	02/11/04	35.3	2400	0.81	25.16
SXDF-N	2	02/11/05	36.2	600	0.79	24.22
SXDF-N	3	02/11/10	41.3	2340	1.03	24.93
SXDF-N	4	03/09/27	362.4	4860	0.71	25.99
SXDF-S	1	02/11/04	35.4	2400	0.77	25.11
SXDF-S	2	02/11/05	36.3	600	0.81	24.18
SXDF-S	3	02/11/10	41.4	2700	0.85	24.97
SXDF-S	4	03/09/22	357.7	4800	0.69	25.61
SXDF-E	1	02/11/04	35.4	2280	0.71	25.26
SXDF-E	2	02/11/05	36.3	1200	1.07	24.42
SXDF-E	3	02/11/10	41.4	4440	0.85	25.32
SXDF-E	4	03/09/26	361.5	4800	0.69	25.81
SXDF-W	1	02/11/04	35.6	2700	0.81	25.19
SXDF-W	2	02/11/05	36.4	750	0.75	24.37
SXDF-W	3	02/11/10	41.6	6210	1.05	25.41
SXDF-W	4	03/09/27	362.4	4800	0.69	25.92

^a Only observations taken during 2002 contribute the number of epochs in each filter.

^b Observed date in yy/mm/dd. When the images were stacked together, all dates for observations are included.

^c Days from the first observation in each field.

^d FWHM of PSF in stacked images

^e Limiting magnitude of 5σ in 2.0 arcsec aperture.

Table 2. Type II supernova templates

Name	Reference	Type	Lightcurve points
SN1979C	DeVaucouleurs et al. 1981 ^a	II-L	23 (U), 32 (B), 31 (V)
SN1980K	Buta 1982 ^b	II-L	20 (U), 25 (B), 25 (V)
SN1998S	Fassia et al. 1998 ^c	II-n	25 (B), 26 (V), 28 (R), 21 (I)
SN1999em	Leonard et al. 2002 ^d	II-P	29 (U), 40 (B), 41 (V), 46 (R), 44 (I)
SN1999gi	Leonard et al. 2002 ^e	II-P	29 (B), 30 (V), 30 (R), 30 (I)
SN2005lb	Sako et al. in prep. ^f	II	1 (<i>u'</i>), 15 (<i>g'</i>), 14 (<i>r'</i>), 12 (<i>i'</i>), 13 (<i>z'</i>)
SN2005lc	Sako et al. in prep. ^f	II	20 (<i>u'</i>), 24 (<i>g'</i>), 24 (<i>r'</i>), 23 (<i>i'</i>), 25 (<i>z'</i>)
SN2006ez	Sako et al. in prep. ^f	II	21 (<i>u'</i>), 21 (<i>g'</i>), 22 (<i>r'</i>), 20 (<i>i'</i>), 22 (<i>z'</i>)
SN2006fg	D'Andrea et al. 2009 ^f	II	13 (<i>u'</i>), 17 (<i>g'</i>), 16 (<i>r'</i>), 17 (<i>i'</i>), 19 (<i>z'</i>)
SN2006fq	D'Andrea et al. 2009 ^f	II	12 (<i>u'</i>), 22 (<i>g'</i>), 22 (<i>r'</i>), 21 (<i>i'</i>), 22 (<i>z'</i>)
SN2006gq	D'Andrea et al. 2009 ^f	II	0 (<i>u'</i>), 18 (<i>g'</i>), 16 (<i>r'</i>), 16 (<i>i'</i>), 13 (<i>z'</i>)
SN2006kg	Sako et al. in prep. ^f	II	20 (<i>u'</i>), 20 (<i>g'</i>), 20 (<i>r'</i>), 20 (<i>i'</i>), 19 (<i>z'</i>)

^a 76-,91-,205-cm telescopes of the McDonald Observatory

^b 76-,91-cm telescopes of McDonald Observatory and 1.55-m telescope of the U.S. Naval Observatory

^c The 82-cm Instituto de Astrofísica de Canarias telescope (IAC80) on Tenerife, the 1.0-m Jacobus Kapteyn Telescope (JKT) on La Palma and the 3.5-m Wisconsin-Indiana-Yale-NOAO telescope (WIYN) at Kitt Peak

^d 76-,91-,205-cm telescopes of the McDonald Observatory

^e The Katzman Automatic Imaging Telescope (KAIT) and the 1.2-m telescope at the Fred Lawrence Whipple Observatory (FLWO).

^f The SDSS's 2.5-meter telescope at Apache Point Observatory

Table 3. SN Ia candidates

Field-ID	SuF02-ID ^a	Offset ^b	RA	Dec	Host ID	z_{phot}	z_{spec}	z_{SN}^c	The allocation of SN Ia to each bin ^d				M_B^e	$m_{i'}$	s^f	Day ^g
									0.2–0.6	0.6–1.0	1.0–1.4	1.4–				
1-018	SuF02-007	11.944	02:18:52.178	-05:01:13.17	iC-083788	0.85	-	0.950	0.028	0.650	0.313	0.009	-18.5	24.7	1.15	32
1-020	SuF02-012 ^{h2,3}	0.205	02:18:51.576	-04:47:25.97	iC-176827	1.15	1.290	1.290	-	-	1.000	-	-19.3	25.1	1.15	34
1-038	SuF02-J02	2.490	02:18:42.854	-05:04:12.50	iC-063533	0.70	0.652	0.652	-	1.000	-	-	-17.9	24.5	1.10	36
1-045	SuF02-082	4.756	02:18:40.690	-05:03:43.73	iC-065953	0.65	0.625	0.625	-	1.000	-	-	-17.8	24.5	1.20	52
1-076		7.785	02:18:31.195	-05:01:23.60	iC-081825	0.75	-	0.750	-	0.985	0.015	-	-19.0	23.6	1.20	18
1-090		3.360	02:18:22.051	-04:57:18.78	iC-107586	0.85	-	0.850	-	1.000	-	-	-18.2	24.7	1.20	14
1-120	SuF02-004	0.378	02:18:09.026	-04:54:18.71	iC-126749	1.00	1.187	1.187	-	-	1.000	-	-19.6	24.6	1.20	30
1-157		2.550	02:17:50.203	-05:03:45.62	iC-066598	0.45	-	0.450	0.993	0.007	-	-	-18.8	22.8	0.75	70
1-175	SuF02-000 ^{h3}	2.953	02:17:42.590	-05:06:33.76	iC-049015	0.75	0.921	0.921	-	1.000	-	-	-18.9	24.2	1.15	44
1-192	SuF02-065 ^{h1}	1.800	02:17:34.589	-05:00:16.78	iC-088216	0.58	1.181	1.181	-	-	1.000	-	-18.7	25.5	1.20	38
1-193	SuF02-060 ^{h1}	1.044	02:17:34.565	-04:53:47.36	iC-129501	1.05	1.063	1.063	-	-	1.000	-	-19.3	24.2	1.00	44
1-202		1.496	02:17:32.114	-04:53:30.42	iC-131867	1.05	-	1.100	-	0.094	0.906	-	-18.9	24.9	0.75	52
1-203		5.611	02:17:32.160	-05:11:15.69	iC-017504	0.90	-	0.900	-	0.998	0.002	-	-19.1	24.0	1.10	0
1-242	SuF02-002	2.535	02:17:12.264	-04:55:08.82	iC-121417	0.75	0.823	0.823	-	1.000	-	-	-18.6	24.2	1.00	36
1-252		1.502	02:17:10.188	-04:50:43.91	iC-148634	0.95	-	0.950	-	0.945	0.054	-	-18.4	24.8	1.20	60
1-254		0.608	02:17:09.758	-04:57:47.89	iC-105194	0.95	-	0.950	-	0.906	0.094	-	-19.5	23.7	0.95	8
1-258	SuF02-071 ^{h3}	8.003	02:17:08.772	-05:02:06.24	iC-076434	0.90	0.928	0.928	-	1.000	-	-	-19.3	23.8	0.95	36
1-280	SuF02-027 ^{h3}	2.005	02:17:00.074	-04:58:20.14	iC-100962	0.60	0.594	0.594	1.000	-	-	-	-19.0	23.2	1.00	38
2-019	SuF02-026	1.720	02:18:51.905	-04:46:57.29	iN-013001	0.35	-	0.800	0.013	0.969	0.015	0.003	-17.5	25.2	0.75	24
2-033 ^j		17.026	02:18:42.509	-04:34:17.99	iN-090581	0.35	-	0.400	1.000	-	-	-	-19.2	22.1	0.90	54
2-042		4.048	02:18:31.850	-04:25:13.52	iN-149479	0.65	-	0.650	0.416	0.584	-	-	-18.7	23.7	1.15	-4
2-138 ^j		0.752	02:17:46.010	-04:36:46.59	iN-077467	1.00	-	1.000	0.002	0.532	0.464	-	-18.7	24.7	1.20	48
2-146 ^j	SuF02-037	1.444	02:17:43.363	-04:30:57.22	iN-113117	0.85	0.924	0.924	-	1.000	-	-	-18.9	24.3	1.10	38
2-167 ^j	SuF02-05	8.014	02:17:27.401	-04:40:45.42	iN-052480	0.85	-	0.850	-	0.970	0.021	0.009	-17.8	25.1	0.90	38
2-175		0.250	02:17:18.859	-04:30:26.53	iN-116245	1.00	-	1.000	-	0.243	0.757	-	-18.3	25.1	1.15	14
3-008 ^j		0.294	02:19:04.080	-05:14:50.16	iS-162495	0.90	-	0.900	-	0.995	0.005	-	-18.4	24.7	1.20	56
3-156		4.336	02:17:48.098	-05:27:44.54	iS-074610	0.65	-	0.650	0.004	0.996	-	-	-18.8	23.6	1.15	66
4-083		11.480	02:20:13.834	-05:07:34.27	iE-135660	1.30	-	1.300	-	0.000	0.996	0.004	-19.1	25.3	1.05	38
4-105 ^j		3.613	02:20:05.904	-05:05:31.83	iE-123124	0.95	-	0.950	-	0.608	0.281	0.111	-18.2	25.0	0.90	52
4-106 ^j		4.766	02:19:26.021	-05:05:06.94	iE-059305	1.00	-	0.950	-	0.747	0.253	-	-18.7	24.5	0.75	54
4-117 ^j		1.345	02:20:16.889	-05:03:50.67	iE-141288	0.95	-	0.950	-	0.999	0.001	-	-19.9	23.1	1.20	8
4-150		13.697	02:19:35.458	-04:57:42.26	iE-076200	3.00	-	0.300	1.000	-	-	-	-17.6	23.1	0.75	-6
4-174 ^j		0.538	02:19:10.296	-04:54:19.19	iE-036303	1.10	-	1.050	-	0.006	0.994	-	-19.9	23.6	0.95	12
4-203		0.024	02:20:32.179	-04:49:58.86	iE-157248	0.95	-	0.950	-	0.666	0.334	-	-18.6	24.6	1.10	64
4-233		0.415	02:19:49.937	-04:45:53.30	iE-097735	0.80	-	0.850	-	1.000	-	-	-19.1	23.7	0.75	70
5-029 ^j	SuF02-025 ^{h1}	0.722	02:16:23.947	-04:49:29.51	iW-069337	0.55	0.606	0.606	-	1.000	-	-	-19.1	23.1	1.05	54
5-035		1.244	02:16:46.918	-04:51:21.98	iW-036122	1.00	-	1.000	-	0.579	0.421	-	-18.6	24.8	0.85	62
5-049 ^j		5.846	02:16:50.143	-04:54:33.53	iW-032007	1.00	1.094	1.094	-	-	1.000	-	-19.3	24.5	0.80	54
5-149 ^j	SuF02-017 ^{h1}	20.365	02:16:45.530	-05:09:48.28	iW-038187	0.50	1.030	1.030	-	-	1.000	-	-18.9	24.5	1.00	30

Table 3. (Continued.)

Field-ID	SuF02-ID ^a	Offset ^b	RA	Dec	Host ID	z_{phot}	z_{spec}	z_{SN}^c	M_B^e	$m_{i'}$	s^f	Day ^g
Candidates rejected as AGN or SN Ib/c, and one possible SN Ia at $z > 1.4$												
1-081 ^l		1.134	02:18:29.273	-05:01:05.60	iC-083570	1.450	-	1.450	-19.5	25.3	0.95	62
1-143 ⁱ	SuF02-058	0.047	02:17:59.674	-04:52:26.77	iC-138418	2.600	-	0.50	-17.7	24.1	1.20	56
2-038 ^k	SuF02-077	2.736	02:18:35.210	-04:26:39.90	iN-140425	0.450	-	0.450	-17.6	24.0	0.90	48
3-202 ^{i,j}	SuF02-061	0.192	02:17:22.769	-05:16:56.58	iS-148873	0.700	1.085	1.100	-19.7	24.0	0.85	22
4-100 ^k		0.347	02:19:56.690	-05:05:55.86	iE-108255	0.750	-	0.750	-18.2	24.3	1.10	54

^a The IDs correspond to the spectroscopic candidates in the other papers (see Lidman et al. 2005, Morokuma et al. 2010, and Suzuki et al. 2012).

^b The offset means distance (pixel) from objects to the center of the host galaxy.

^c The redshifts are estimated by the light curve fitting with photometric redshifts of host galaxies. When available, the spectroscopic redshifts are used.

^d The allocation of SN Ia to $0.2 < z < 0.6$, $0.6 < z < 1.0$, $1.0 < z < 1.4$, and 1.4 bins according to $PDF(z)$ (see §3.1.6)

^e The absolute magnitudes are not corrected for extinction from SN host galaxies.

^f The stretch factors are not B -band stretch but just observed i' -band stretch used in the light curve fitting.

^g The days means the dates from the peak magnitude.

^h Spectroscopically confirmed SNe Ia (including probable Ia). The numbers represent the reference: 1 is published in Lidman et al. (2005), 2 is published in Morokuma et al. (2010), and 3 is going to be included in Rubin et al. (in prep.)

ⁱ Detected in X-rays with XMM-Newton.

^j Candidates with color information (detected in R_c , i' and z')

^k Failed color cut.

^l This object at $z = 1.45$ is not included in the rate calculation.

Table 4. Summary of systematic uncertainties in percent

Source items	num./denom. ^a	$0.2 \leq z < 0.6$	$0.6 \leq z < 1.0$	$1.0 \leq z < 1.4$
(1) Ratio of IIP and IIL	numerator	+0.6 -0.3	+0.8 -0.4	+0.8 -0.4
(2) Luminosity function of SN II	numerator	+0.3 -0.6	+1.4 -1.4	+1.1 -0.9
(3) Discrimination of Type Ib/c	numerator	+22.6 -45.5	+6.2 -12.4	+0.4 -0.8
(4) AGN contamination	numerator	+0.0 -2.6	+0.0 -2.6	+0.0 -2.6
(5) CC SN contamination at high-z	numerator	-	-	+0.0 -8.0
(6) Evolution effect of SNe Ia	denominator	+0.5 -0.0	+3.2 -0.0	+14.5 -0.0
(7) Extinction (known)	denominator	+0.0 -2.9	+0.0 -6.5	+0.0 -11.9
Total known systematics		+22.6 -45.7	+7.1 -14.3	+14.5 -14.7
(7)' Extinction (unknown)	denominator	+50.0 -0.0	+50.0 -0.0	+50.0 -0.0
Total known and unknown dust systematics		+54.9 -45.7	+50.5 -14.3	+52.1 -14.7

^a “numerator” and “denominator” refer to those of Equation 4.**Table 5.** The SN Ia rates in SXDF

Redshift bin	z_{eff}^a	SNR ^b	error(stat)	error(sys) ^c	Denom. ^d	N_{est}^e	N_{II}^f	$N_{Ib/c}^g$	N_{comp}^h	N_{Ia}^i
$0.2 \leq z < 0.6$	0.44	0.262	+0.229 -0.133	+0.059+0.131 -0.120	13.179	4.46	0.61	1.18	0.78	$3.45^{+3.02}_{-1.76}$
$0.6 \leq z < 1.0$	0.80	0.839	+0.230 -0.185	+0.060+0.419 -0.120	24.199	22.48	2.52	1.88	2.23	$20.31^{+5.58}_{-4.47}$
$1.0 \leq z < 1.4$	1.14	0.705	+0.239 -0.183	+0.102+0.352 -0.103	20.442	12.09	0.91	0.09	3.32	$14.41^{+4.88}_{-3.75}$

^a Effective redshift.^b Supernova rates are given in units $10^{-4} h_{70}^3 yr^{-1} Mpc^{-3}$.^c Known systematic, followed by *ad hoc* uncertainty due to dust.^d Denominator of Equation 4 in units $10^4 h_{70}^{-3} yr Mpc^3$.^e Estimated numbers of observed SNe Ia (see §4).^f Estimated number of contaminating Type II SNe.^g Estimated number of contaminating Type Ib/c SNe after removing two objects classified as SN Ib/c, i.e., 2-038 and 4-100.^h Estimated number due to SN typing incompleteness.ⁱ The number of SN Ia used in the rate calculation. The errors show statistical uncertainty.